REDUCED-ORDER MODELING TOWARD SOLVING INVERSE PROBLEMS IN SOLID MECHANICS AND FLUID DYNAMICS

by

Mohammad Ahmadpoor

BS in Mechanical Engineering, Amirkabir University of Technology,

Iran, 2011

Submitted to the Graduate Faculty of

the Swanson School of Engineering in partial fulfillment

of the requirements for the degree of

Doctor of Philosophy

University of Pittsburgh

2016

UNIVERSITY OF PITTSBURGH

SWANSON SCHOOL OF ENGINEERING

This dissertation was presented

by

Mohammad Ahmadpoor

It was defended on

March 29th, 2016

and approved by

John C. Brigham, PhD, Associate Professor, Department of Civil and Environmental Engineering and Bioengineering

Mark Kimber, PhD, Associate Professor, Department of Nuclear Engineering

Andrew P. Bunger, PhD, Assistant Professor, Department of Civil and Environmental Engineering

Jeen-Shang Lin, PhD, Associate Professor, Department of Civil and Environmental Engineering

Dissertation Director: John C. Brigham, PhD, Associate Professor, Department of Civil and Environmental Engineering and Bioengineering

REDUCED-ORDER MODELING TOWARD SOLVING INVERSE PROBLEMS IN SOLID MECHANICS AND FLUID DYNAMICS

Mohammad Ahmadpoor, PhD

University of Pittsburgh, 2016

Despite great improvements in computing hardware and developments of new methodologies for solving partial differential equations (PDEs), solving PDEs numerically can still be computationally prohibitive for certain applications. This computational difficulty is especially true when the solution of PDEs is tied to characterization, control, design, or other inverse problems in general. Most of the traditional PDE solution strategies, such as the Finite Element Method or Finite Volume Method can require hundreds of thousands of degrees of freedom to accurately capture the behavior of even relatively simple physical system. The computational cost is several orders of magnitude higher for solving optimization problems (a common approach to solve inverse problems), which require obtaining several solution fields. Hence, model order reduction is necessary to enable the solution of such optimization problems with sufficient efficiency to allow practical applicability. Several approaches have been developed to create accurate reduced-order models (ROMs) of physical systems with dramatically reduced computational expense. Yet, several questions remain as to the optimal approach to create ROMs for a given physical system to ensure suitable accuracy, and even more so in relation to inverse problem applications. The objective of the present work is to address issues relating to the creation of suitably accurate ROMs that can be utilized for the solution of a variety of computational inverse mechanics problems. This work focuses on ROMs that utilize proper orthogonal decomposition (POD) to create a reduced-order basis for the PDE solution from a set of previously obtained potential solution fields (i.e., snapshots) of the system of interest. First, a generally applicable algorithm is presented to

efficiently create accurate ROMs for use in solving inverse problems in material characterization (i.e., nondestructive evaluation). This algorithm is based upon a novel concept for maximizing the diversity of the system snapshots used to create the ROM. Results show that by maximizing the snapshot diversity, the accurate generalization of the resulting ROM is substantially improved, which then improves inverse problem solution capabilities. Then, a comprehensive study is presented of the capability of a set of different approaches for reduced-order modeling (all still using POD) to represent systems involving flow past bluff bodies. One of the relatively unexplored issues when creating ROMs for fluid flows is the accuracy with respect to changes in Reynolds (Re) number. The present work uses the generalized POD technique to create ROMs that are capable of predicting flow field not only at different time levels, but also at different Re numbers. Finally, the ROM strategies explored for fluid flow were extended to investigate the applicability to optimal flow control problems. The ROM of flow was used along with an optimization technique and adjoint method for gradient calculation to solve a control problem to reduce the drag force in flow past one or more cylinders. Results of the solution of this optimal control problem show that the developed ROMs are capable of solving complex optimization problems with significantly reduced computational expense.

TABLE OF CONTENTS

LIST OF TABLES

LIST OF FIGURES

PREFACE

I would like to thank my advisor Dr. John C. Brigham for his continuous help and support during my years at Pitt.

I would like to thank Dr. Mark Kimber, Dr. Andrew P. Bunger, and Dr. Jeen-Shin Lin for serving on my graduate committee and for their support throughout my studies.

I also would like to thank my colleagues in Professor John C. Brighm's group for their help and encouragement during my PhD study especially Dr. Bahram Notghi.

I would like to dedicate this Doctoral dissertation to my parents, Hassan Ahmadpoor and Ommolbanin Noshirvani, who are the only reason that I was able to pursue my studies.

1.0 A GENERALIZED ITERATIVE APPROACH TO IMPROVE REDUCED-ORDER MODEL ACCURACY FOR INVERSE PROBLEM APPLICATIONS

1.1 ABSTRACT

A generally applicable algorithm for iterative generation of data ensembles to efficiently create accurate computational mechanics reduced-order models (ROM) for use in computational approaches to approximate inverse problem solutions is presented and numerically evaluated. The ROM approach considered is based on identifying the optimal low-dimensional basis to be used within a Galerkin weak-form finite element method to provide substantially reduced computational cost while maintaining accuracy relative to that of a (traditional) full-order finite element model. Furthermore, proper orthogonal decomposition is used to derive the ROM basis from a set of response fields (i.e., snapshots) generated *a priori* with full-order finite element analyses. Therefore, the set of full-order finite element analyses used to create the ROM directly affects the accuracy/generalization of the ROM. The core hypothesis of the algorithm presented is that maximizing the diversity, as defined in a measurable sense, of the full-order models used to create the ROM will improve the accuracy of the ROM over a range of input system parameters. Based on an initial (small) set of snapshots, the algorithm uses snapshot correlation to quantify the snapshot diversity with respect to the system input parameters. Then, the algorithm iteratively applies surrogate-model optimization to identify the next set(s) of system input parameters to be evaluated with full-order analyses to create additional "optimal" snapshots. Although generally applicable to a variety of physical processes, the ROM approach with the iterative snapshot generation algorithm is presented within the context of steady-state dynamic solid mechanics of heterogeneous media. Two

simulated case studies are then presented involving forward analysis and inverse characterization of semi-localized Youngs modulus distributions in structural components as could be relevant to nondestructive evaluation problems. The iterative snapshot generation algorithm is shown to produce ROMs that can accurately estimate displacement response fields over a wide range of material parameters, and which are substantially more accurate than ROMs created from randomly generated snapshot sets. Moreover, the accurate generalization of the iteratively generated ROMs is shown to be sufficient to consistently produce accurate inverse characterization solution estimates with a fraction of the computational expense that would be required to do so with full-order analyses.

1.2 INTRODUCTION

There are a wide range of efforts covering almost every engineering field seeking to continually develop and improve methods for the solution of inverse problems relating to the mechanics of structures and system, including design, control, and characterization of system properties at many different scales and involving many different physical processes [110, 6]. However, often at the core of these efforts is the nearly omnipresent ill-posedness, with these inverse problems suffering from some level of solution non-uniqueness, non-existence, and/or instability. One result of this ill-posedness is that surrogate mappings of the inverse relationship or other such attempts to directly connect components of the desired or measured forward response to system (inverse problem) unknowns are often inapplicable in the general quantitative case. Therefore, computational inverse problem solution approaches (i.e. computational inverse mechanics approaches) that combine computational forward mechanics with optimization methods are often the only feasible solution strategy. Several computational inverse mechanics approaches have been developed in recent years for a variety of applications, including estimation of thermal material properties (e.g., [6, 7, 9, 2, 3]), structural characterization and/or damage detection (e.g., [3, 17, 47, 92, 107]), microstructural design (e.g., [41, 113, 1]), and optimal control (e.g., [30, 88, 76, 56, 32]).

The typical approach to computational inverse problem solution methods is to combine a numerical representation of the system being considered with a nonlinear optimization technique to identify the properties that minimize some measure of the difference between the numerical representation and the experimental measurements (or desired behavior). Without accurate forward modeling, an inverse solution may be unattainable, or worse yet, any apparent solution may be dramatically incorrect. Even with the continued advancements in computing processors and grid-computing capabilities, there is still a significant need to reduce the associated computational costs for these inverse problem solution approaches. Therefore, while implementing the highest resolution multiphysics modeling possible will provide for the optimal solution accuracy, the resulting computational expense is expected to cause most realistic inverse applications to become infeasible.

To address the issues of computational expense, many currently employed inverse problem solution approaches either reduce the model size through assumptions about the nature of the system response (e.g., [72, 12, 70, 69]),which simplifies the nature of the inverse problem search space and leads to fewer required forward simulations (e.g., [98]), but may be impractical for some applications.

More generally, in computational forward modeling several approaches have been developed to create accurate numerical models of physical systems with dramatically reduced computational expense. Most recent developments(as will be applied in the present work) do not replace the physics-derived governing equations of the system, as is the case for surrogate- (i.e. meta-) model methods [18, 89], but rather seek to identify a basis that is optimally incorporated into a numerical method to solve the governing equations (e.g., as the approximation functions for the weak-form Galerkin method) [5]. Therefore, similar to typical FE (Finite Element) approaches, these reduced order models (ROMs) are capable of approximating whatever physical process is desired (not just structural mechanics behavior), still include the physics of the given boundary value problem, and are not necessarily dependent on one specific set of system inputs such as an initial constitutive model (as in modal superposition). By using a global approximation, ROMs can have orders of magnitude fewer degrees of freedom than traditional FE methods, which dramatically reduces the computa-

tional expense to obtain forward numerical solutions, yet are often simple to implement into existing computational mechanics codes.

Although they are not often both addressed, in general there are two fundamental steps for most approaches to create bases for ROMs: (1) acquisition of an ensemble of possible solution fields for the system under consideration and (2) data processing of the ensemble to create a basis. Most commonly the focus is placed on the data processing (Step (2)), and the ensemble, which can be obtained experimentally or numerically, is assumed to be given in some sense. For example, the proper orthogonal decomposition (POD) method (in some cases interchangeably referred to as Karhunen-Loeve transform or principal component analysis) is one such processing method that has been used in several examples to process ensemble data to produce ROMs, and has been shown in many cases to provide bases for accurate numerical representations for complex systems with minimal computational cost [46, 48, 65, 23]. POD has also been applied to several ROMs within inverse problem solution methodologies, such as optimal control [88, 76, 8, 59], microstructural design [1], and nondestructive testing and system identification [11, 40, 53, 57, 84, 18]

As stated, relatively little work has been done thus far to specifically develop methods for generating the necessary data ensembles with a limited number of full-order analyses (e.g. traditional FE analyses of the system) that will lead to optimally accurate ROMs. Furthermore, the majority of this previous work has been focused on *a priori* sampling strategies, that define a fixed distribution of the values in the parameter space based upon the physical bounds on the parameters and the total number of snapshots to be generated with these parameter values. Several of these studies have considered ROM accuracy alone (i.e., not in the context of inverse problem solution capabilities) with respect to purely mathematical sampling strategies (i.e., not considering the physics of the problem in determining the sampling), including Latin hypercube sampling [78] and centroidal voronoi tessellation sampling [31, 91], which have shown varying improvements in performance (accuracy and/or efficiency) when compared to random, uniform, and/or other *a priori* sampling techniques. One of the few examples that has explored in detail the effect of ensemble generation on inverse solution strategies with ROMs is [51], which showed for a damage identification inverse problem that using *a priori* sampling to create an ensemble by uniformly varying the damage parameters

lead to as good, and many times better, inverse identification capabilities than a random sampling. Alternatively, [18] attempted to take into account the physics of the problem of interest, and hypothesized and tested an approach for "maximum diversity" to optimally derive an ROM ensemble *a priori* for inverse problems to characterize rate-dependent solid material behavior. However, while they are straightforward approaches, many of the *a priori* sampling approaches (particularly those closest to uniform sampling) can require an excessive number of samples (beyond the feasible limit on evaluations in some cases) to sufficiently cover the parameter space. Moreover, there is naturally a fundamental limitation in only considering *a priori* sampling, particularly without any consideration of the physics of the model as related to the parameters being sampled [73]. With these *a priori* techniques there is no problem-specific reasoning for the choice of the samples, leading to the potential for significant samples being overlooked or a large number of samples being required for accuracy. In contrast, iterative sampling approaches seek to incrementally select the next best sample(s) based on problem-related information that can be derived from the ensemble that has been evaluated to that point in the procedure. One of the few examples of an iterative sampling approach is the certified reduced basis methods [97, 96, 86] that center on the use of *a posteriori* error estimates for ROMs. These certified reduced basis methods attempt to create the least number of ensemble members through full-order numerical analyses to suitably bound the error estimate. This approach could potentially provide an elegant means to create and/or update a ROM basis to be optimal (for the given order) by choosing simulation parameters for new ensemble members that have the highest *a posteriori* error estimate, and would thus most significantly reduce the error estimate for the subsequent updated ROM. However, this approach hinges on the ability to generate the *a posteriori* error estimate for the ROM, which is nontrivial to determine. Moreover, the assumption that the optimal ensemble member has the maximum *a posteriori* error estimate for the current basis may not be true for all cases.

This work presents a novel generally applicable algorithm for the iterative generation of a data ensemble that can be used to create a ROM such that the accuracy of the ROM is improved over a range of input system parameters. The algorithm is based upon the assumption that maximizing the diversity of the data ensemble within the space of variable

system input parameters will improve the generalization of the resulting ROM over the space of input parameters, and thus improve the capabilities of the ROM within a computational inverse problem solution method. Section 1.3 outlines the details of the iterative data ensemble and reduced-order modeling strategy within the context of POD ROMs for steady-state dynamic solid mechanics of heterogeneous solids. Then, Section 1.4 presents and discusses a series of numerical examples displaying the capabilities of the ROM generation strategy in terms of both forward modeling accuracy and inverse problem solution capabilities, which is followed by the concluding remarks in Section 1.5.

1.3 OPTIMAL BASIS GENERATION FOR REDUCED-ORDER MODELING

The following discussion of an approach to create optimally accurate physics-based reduced-order models is presented within the context of steady-state harmonic solid mechanics of heterogeneous solids with a range of potential material parameters. Such a reduced-order model could be particularly applicable to a computational solution procedure for an inverse problem relating to characterization or design of the heterogeneous material properties for a solid that is tested or utilized with some type of harmonic excitation (e.g., [17, 18, 83] [109]. By providing high accuracy and low computational cost predictions of the system response over the range of potential material properties, an inverse solution procedure would be able to relatively quickly search through the potential solutions to identify an accurate estimate of the true (or optimal) material properties. However, a critical point is that the concepts presented are intended to be generalizable to a wide variety of applications. As stated the reduced-basis reduced-order modeling approach has been shown to be applicable to a wide variety of boundary value problems for a variety of physical systems, including not just solid mechanics, but also heat transfer and fluid mechanics, among others, and the basis generation approach is implementable for any one of these applications. More importantly, the optimal basis generation approach is applicable to generate an optimal basis with respect to a wide variety of variable system inputs, including material properties (as discussed herein) and

boundary conditions, and is independent of their parameterization (i.e., the basis generation algorithm can be used with whatever parameters control the variable/unknown input of the model).

1.3.1 Steady-State Solid Mechanics Governing Equations and Weak Form

Assuming that the solid considered is excited harmonically to a steady-state, and therefore the system variables vary harmonically in time with angular frequency ω, and neglecting body forces, the governing equations and boundary conditions (i.e., boundary value problem) from conservation of momentum can be written as:

$$\nabla \cdot \boldsymbol{\sigma}(\vec{x},\omega) + \omega^2 \rho(\vec{x}) \vec{u}(\vec{x},\omega) = \vec{0}, \quad \forall \vec{x} \in \Omega, \tag{1.1}$$

$$\boldsymbol{\sigma}(\vec{x},\omega) \cdot \vec{n}(\vec{x}) = \vec{T}(\vec{x},\omega), \quad \forall \vec{x} \in \Gamma_T, \tag{1.2}$$

and

$$\vec{u}(\vec{x},\omega) = \vec{u}^0(\vec{x},\omega), \quad \forall \vec{x} \in \Gamma_U, \tag{1.3}$$

where $\vec{x}$ is the spatial position vector, $\boldsymbol{\sigma}(\vec{x},\omega)$ is the stress tensor, $\rho(\vec{x})$ represents the density of the solid, $\vec{u}(\vec{x},\omega)$ is the steady-state displacement amplitude field, $\vec{T}(\vec{x},\omega)$ is the applied traction amplitude vector, $\vec{u}^0(\vec{x},\omega)$ is the applied displacement amplitude, Ω is the domain of the solid, $\vec{n}(\vec{x})$ is the unit outward normal vector to the surface of the domain, Γ, and Γ_T and Γ_U are the portions of the domain surface where traction and displacement are applied, respectively, such that $\Gamma_T \bigcup \Gamma_U = \Gamma$ and $\Gamma_T \bigcap \Gamma_U = \varnothing$. Assuming for simplicity small strain linear elastic behavior, the constitutive equations can be written as:

$$\boldsymbol{\sigma}(\vec{x},\omega) = \boldsymbol{C}^{IV} : \boldsymbol{\epsilon}(\vec{x},\omega), \tag{1.4}$$

with

$$\boldsymbol{\epsilon}(\vec{x},\omega) = \frac{1}{2}\left(\nabla \vec{u}(\vec{x},\omega) + \nabla \vec{u}(\vec{x},\omega)^T\right) \tag{1.5}$$

where $\boldsymbol{\epsilon}$ is the standard small strain tensor and $\boldsymbol{C}^{IV}$ is the fourth-order elasticity tensor.

The standard weak form Galerkin approach [90] was employed herein to approximate the solution of the boundary value problem described by Eqs. (1.1)-(1.5) using an arbitrary

approximation function of the steady-state harmonic displacement field. As such, the weak form of the steady-state dynamic solid mechanics problem can be expressed as:

$$\int_{\Omega} \nabla \delta\vec{u}(\vec{x}) : \boldsymbol{\sigma}(\vec{x},\omega) d\vec{x} - \int_{\Omega} \omega^2 \rho(\vec{x}) \delta\vec{u}(\vec{x}) \cdot \vec{u}(\vec{x},\omega) d\vec{x} - \int_{\Gamma_T} \delta\vec{u}(\vec{x}) \cdot \vec{T}(\vec{x},\omega) d\vec{x} = 0, \quad (1.6)$$

where $\delta\vec{u}(\vec{x})$ is an arbitrary weight function vector that satisfies $\delta\vec{u}(\vec{x}) = 0, \forall x \in \Gamma_u$. Therefore, all that is necessary to complete the Galerkin approach is to substitute an approximation for the displacement field and the weight function (using the same basis for both) to obtain a discretized form and a linear system of equations for each excitation frequency. The common finite element approach would be to discretize the spatial domain into elements and use polynomial approximations within each element to discretize then assemble a system of equations. However, as is commonly known, this finite element approach (referred to as the full-order modeling approach herein) typically requires at least many thousands of degrees of freedom, even for relatively simple two-dimensional problems to accurately represent the physics of the system. Alternatively, as stated in the introduction, the objective of the reduced-basis form of reduced-order modeling is to identify a basis that is optimal in some sense for representing the physics of the system under consideration with far fewer degrees of freedom than the full-order model. One such approach to generating a reduced-basis is through POD, and implementing this basis for reduced-order modeling is detailed in the following.

1.3.2 Reduced-Order Modeling with Proper Orthogonal Decomposition

The core hypothesis of the reduced-basis reduced order modeling approach considered in the present work is that a relatively small number of full-order (i.e., traditional finite element) analyses based upon different values of the input parameters of interest (material parameters herein) contain fundamental information about the potential solution fields of the BVP (Boundary Value Problem) and can be used to derive a low-dimensional basis that can predict the solution fields for a range of input parameters (not just the specific parameter values used to generate the set of full-order analyses) with reasonably sufficient accuracy. The POD approach specifically derives the low-dimensional basis such that the difference

between the original full-order data and the best approximation to that data with this basis is minimized in an L_2 average sense. Thus, the problem to determine the POD basis can be cast as an optimization problem to determine the set of m modes $\{\phi_i(\vec{x})\}_{i=1}^m$ given a set of n full-order analysis fields (where generally m is much smaller than n) $\{u(\vec{x},\vec{\gamma}_k)\}_{k=1}^n$, for each variation of the input parameters of interest $\vec{\gamma}_k$, such that:

$$\underset{\{\phi_i(\vec{x})\}_{i=1}^m \in L_2(\Omega)}{\text{Minimize}} \left\langle \|\vec{u}(\vec{x},\vec{\gamma}_k) - \vec{\hat{u}}(\vec{x},\vec{\gamma}_k)\|^2_{L_2(\Omega)} \right\rangle, \tag{1.7}$$

where:

$$\langle \vec{u}_k \rangle = \frac{1}{n}\sum_{k=1}^{n} \vec{u}_k, \tag{1.8}$$

$$\|\vec{u}(\vec{x})\|^2_{L_2(\Omega)} = (\vec{u}(\vec{x}), \vec{u}(\vec{x}))\,, \tag{1.9}$$

$$(\vec{u}(\vec{x}), \vec{v}(\vec{x})) = \int_\Omega \vec{u}(\vec{x}) \cdot \vec{v}(\vec{x}) d\vec{x}, \tag{1.10}$$

and assuming an orthonormal basis, the best approximation can be defined by the projection onto the basis as:

$$\vec{\hat{u}}(\vec{x},\vec{\gamma}_k) = \sum_{i=1}^{m} \left(\vec{\phi}_i(\vec{x}), \vec{u}(\vec{x},\vec{\gamma}_k)\right)\vec{\phi}_i(\vec{x}). \tag{1.11}$$

Through several manipulations, including applying the method of snapshots, the POD optimization problem defined by Eq. (1.7) can be transformed into the following n-dimensional eigenvalue problem (see [18] and the references therein for additional details on the POD formulation):

$$\frac{1}{n}\sum_{k=1}^{n} A_{jk} C_k = \lambda C_j, \tag{1.12}$$

where

$$A_{jk} = \int_\Omega \vec{u}(\vec{x},\vec{\gamma}_j) \cdot \vec{u}(\vec{x},\vec{\gamma}_k) d\vec{x}. \tag{1.13}$$

An optimal set of as many as n orthogonal basis functions (i.e., POD modes) can then be determined from the solution of the above eigenvalue problem by:

$$\vec{\phi}_i(\vec{x}) = \frac{1}{\lambda^{(i)} n}\sum_{k=1}^{n} \vec{u}(\vec{x},\vec{\gamma}_k) C_k^{(i)}, \quad \text{for } i = 1, 2, ..., n, \tag{1.14}$$

where $C_k^{(i)}$ is the k^{th} component of the i^{th} eigenvector from the solution of (1.12) and $\lambda^{(i)}$ is the corresponding eigenvalue. $\lambda^{(i)}$ is often considered a measure of the "importance of the corresponding mode" ($\vec{\phi}_i(\vec{x})$) for approximating the given dataset of potential solution fields. Therefore, a common procedure (as was done herein) is to only use the m modes with the highest corresponding eigenvalues, with $m < n$, for any subsequent solution approximation, and the remaining modes are discarded (a typical heuristic is to use the set with corresponding eigenvalues that represent around 99% of the total sum of the n eigenvalues).

The m-dimensional basis obtained from applying POD to the given set of full-order analyses can be implemented to create a ROM by simply applying this new low-dimensional basis to approximate the components of the weight function vector and the displacement vector in the weak form shown in Eq. (1.6) as:

$$\delta\vec{u}(\vec{x}) = \sum_{i=1}^{m} d_i \vec{\phi}_i(\vec{x}) \tag{1.15}$$

and

$$\vec{u}(\vec{x}, \vec{\gamma}) = \sum_{i=1}^{m} a_i(\vec{\gamma})\vec{\phi}_i(\vec{x}), \tag{1.16}$$

where d_i are the arbitrary coefficients for the weight functions and $a_i(\vec{\gamma})$ are the coefficients to be determined by the numerical analysis to approximate the displacement response of the system given a new set of system input parameters ($\vec{\gamma}$), such as material parameters and/or excitation frequency. (Note, that in the case of non-homogeneous essential boundary conditions, the approach can be modified slightly by applying POD to the modified snapshots as $\vec{\tilde{u}}(\vec{x}, \vec{\gamma}) = \vec{u}(\vec{x}, \vec{\gamma}) - \langle \vec{u}_k \rangle$, and replacing Eq. 1.16 with $\vec{u}(\vec{x}, \vec{\gamma}) = \langle \vec{u}_k \rangle + \sum_{i=1}^{m} a_i(\vec{\gamma})\vec{\phi}_i(\vec{x})$.)

Eliminating the arbitrary weight function coefficients, the linear system of equations for the reduced-order model to determine the vector of modal coefficients $\{a\}$ can be written as:

$$([K_\phi] - [M_\phi])\{a\} = \{R_\phi\}, \tag{1.17}$$

where

$$[K_\phi] = \int_\Omega [B_\phi]^T [C][B_\phi] d\vec{x}, \tag{1.18}$$

$$[M_\phi] = \int_\Omega \omega^2 \rho(\vec{x})[\Phi]^T[\Phi] d\vec{x}, \tag{1.19}$$

$$\{R_\phi\} = \int_{\Gamma_T} [\Phi]^T \vec{T}(\vec{x}, \omega) d\vec{x}, \tag{1.20}$$

$[\Phi]$ is the matrix of the m POD modes, $[B_\phi]$ is the matrix of derivatives of the POD modes (as needed to calculate the strain using the displacement approximation), and $[C]$ is the material stiffness matrix, assuming a transformation of Eq. (1.6) to Voigt notation. Note that in the general case the amplitude fields could be complex numbers to account for differences in phase (as could be caused by material dissipation, or otherwise), which could be implemented by simply approximating the real and imaginary components independently as shown in Eq. (1.16).

The above derivation of the POD reduced-order modeling follows the standard implementation of the Galerkin weak form finite element method. The only significant difference from the standard finite element approach is that the POD basis approximation is spatially global in this reduced-order model case, rather than defined locally over each individual element in a mesh. More importantly, one critical question still remains unanswered from the above formulation, which is how to select the set of input parameters used to create the set of full-order analyses to then use for creating the POD basis. In particular, this dataset must be generated in such a way to limit the number of full-order simulations necessary to ensure sufficiently accurate generalization of the reduced-order model over the admissible range of the input parameters of interest. The following presents just such an approach to iteratively generate the input parameters that will be used to simulate full-order response fields to create accurate POD reduced-order models. More specifically, this iterative snapshot generation approach seeks to create a set of full-order analyses that captures all significant features of the potential solution fields in the space of the parameters of interest with a limited number of full-order analyses to ensure accurate subsequent reduced-order modeling, or alternatively, to improve the ROM accuracy for a fixed number of full-order analyses.

1.3.3 Iterative Snapshot Generation to Improve Generalization

Extending the work in [18], the core hypothesis of the proposed iterative snapshot generation method is that maximizing the diversity of the snapshots created within the space of

the input parameters of interest will improve the generalization of the resulting reduced-order model over that parameter space. The work in [18] showed that snapshot diversity for viscoelastic material parameters could be (at least in part) quantified with respect to the difference between the material energy dissipation as well as the energy storage defined by the material parameter sets. A metric was presented to quantify this material diversity, and this metric was shown to be capable of creating a diverse set of snapshot fields within the parameter space, which then yielded significantly more accurate reduced-order models compared to randomly generated snapshots for a fixed maximum number of full-order analyses. However, this prior approach is limited in application to viscoelastic material parameters. Alternatively, the present work seeks to establish a generalized approach that is applicable to a wide variety of physical systems and input parameters of interest that will be used to generate snapshots.

The first, most critical step in this approach to optimize snapshot generation is to form a metric that quantifies the diversity of the snapshot fields. One way diversity can be directly quantified for any pair of snapshots (based on the sets of input parameters used to simulate the full-order models $\vec{\gamma}_i$ and $\vec{\gamma}_j$) is through the correlation between the two snapshots as:

$$R(\vec{\gamma}_i, \vec{\gamma}_j) = \frac{|(\vec{u}(\vec{x}, \vec{\gamma}_i), \vec{u}(\vec{x}, \vec{\gamma}_j))|}{\|\vec{u}(\vec{x}, \vec{\gamma}_i)\|_{L_2(\Omega)} \cdot \|\vec{u}(\vec{x}, \vec{\gamma}_j)\|_{L_2(\Omega)}}. \tag{1.21}$$

If this correlation is minimized between all snapshot fields, then the diversity of the set of snapshots could be said to be maximized in some sense. However, this definition of snapshot diversity cannot be used directly to generate a set of snapshots in practice, as it would require full-order analyses to produce the response fields for each set of input parameters to quantify the diversity, which is exactly what is trying to be avoided in an effort to improve computational efficiency with reduced-order modeling. Alternatively, to maintain this direct definition of snapshot diversity, but avoid excessive computational expense, the present work proposes the use of iterative surrogate (i.e., meta) modeling to predict and minimize the snapshot correlation with respect to the input parameters of interest.

Given a set of n_0 input parameters sets $\{\vec{\gamma}_i\}_{i=1}^{n_0}$ and the corresponding full-order analysis response fields (i.e., snapshot), a measure of the total diversity of the i^{th} snapshot (created with input parameter set $\vec{\gamma}_i$) within the set can be calculated as:

$$R^*(\vec{\gamma}_i) = \sum_{\substack{j=1 \\ j \neq i}}^{n_0} R(\vec{\gamma}_i, \vec{\gamma}_j). \tag{1.22}$$

Then, provided with the diversity metric for each snapshot in the set $\{R^*(\vec{\gamma}_i)\}_{i=1}^{n_0}$, the objective of the surrogate model approach is to create an approximate mapping (i.e., surrogate model) between the input parameters and the diversity metric. Any preferred machine learning technique can be used to generate the surrogate model, such as artificial neural networks ([39]) or support vector regression ([104, 44]), with the examples presented herein using support vector regression. The surrogate model of the diversity $R^{SM}(\vec{\gamma})$ can then be easily minimized to estimate the optimal next set of input parameters (within the domain of the parameters X) to use with the full-order model to generate another set of snapshots that would maximize the diversity of the snapshot set, as in:

$$\underset{\vec{\gamma} \in X}{\text{Minimize}} \quad R^{SM}(\vec{\gamma}). \tag{1.23}$$

Note that since the computational cost of the surrogate model is negligible, then essentially any preferred global optimization algorithm can be used, regardless of the algorithm efficiency, with a genetic algorithm [39] being used for the examples herein. Due to the expectation of some loss of accuracy in the surrogate model, an additional constraint on the parameter sets was added to the surrogate model optimization for the present work. To ensure that the input parameter sets are not overly clustered in the parameter space, the new parameter set was constrained to be a specified minimum distance δ from every other parameter set, such that:

$$\|\vec{\gamma} - \vec{\gamma}_i\| > \delta \quad \text{for } i = 1, 2, ..., n_0, \tag{1.24}$$

where $\|\cdot\|$ is the standard l_2-norm. Once the new set of input parameters is determined from the solution of Eq. (1.23) and Eq. (1.24), the input parameter set is used with the full-order model to generate a new snapshot.

Figure 1.1 shows a flowchart that describes the overall procedure for the iterative snapshot generation algorithm to maximize snapshot diversity and as a result improving reduced-order model accuracy. First, an initial set of n_0 input parameter sets is randomly generated from a uniform distribution within the parameter space X, and each set is evaluated with the full-order model to create the initial set of snapshots. The diversity metric is calculated for each snapshot in the set Eq. (1.22), and the surrogate model approach described above is applied to determine the next "best" set of input parameters. A new snapshot is generated with this input parameter set from the surrogate model approach and the corresponding diversity metric is calculated. Lastly, the set of input parameter sets and corresponding diversity metrics is expanded ($\{\vec{\gamma}_i\}_{i=1}^{n_0+1}$ and $\{R^*(\vec{\gamma}_i)\}_{i=1}^{n_0+1}$), and the surrogate model process is repeated until some convergence criteria is reached (e.g., the increase in R^* exceeds a tolerance or a maximum number of full-order analyses has been performed). At the completion of the snapshot generation algorithm a POD reduced-order model can be generated and utilized.

1.4 EXAMPLES AND DISCUSSION

To display the capabilities and potential applicability of the method presented for iterative generation of optimal reduced-order models, two simulated case studies were considered regarding efficient and accurate modeling of the deformation of structural members with semi-localized Young's modulus distributions. Although the concepts presented are intended to be generally applicable to a variety of physical processes/properties and applications, this specific example of solids with locally distributed stiffness was chosen for context based on its potential applicability to nondestructive evaluation applications [83, 25, 60, 4, 21, 29]. Thus, the examples also examined the capabilities to then inversely characterize such material property distributions using a computational inverse solution procedure relying on this modeling. As such, the core question examined throughout the examples is: "Can the iterative approach be used to create a ROM that can produce sufficiently accurate response fields for any feasible set of parameter values for inverse characterization purposes?" In both test cases POD ROMs were generated through the iterative approach to maximize diversity

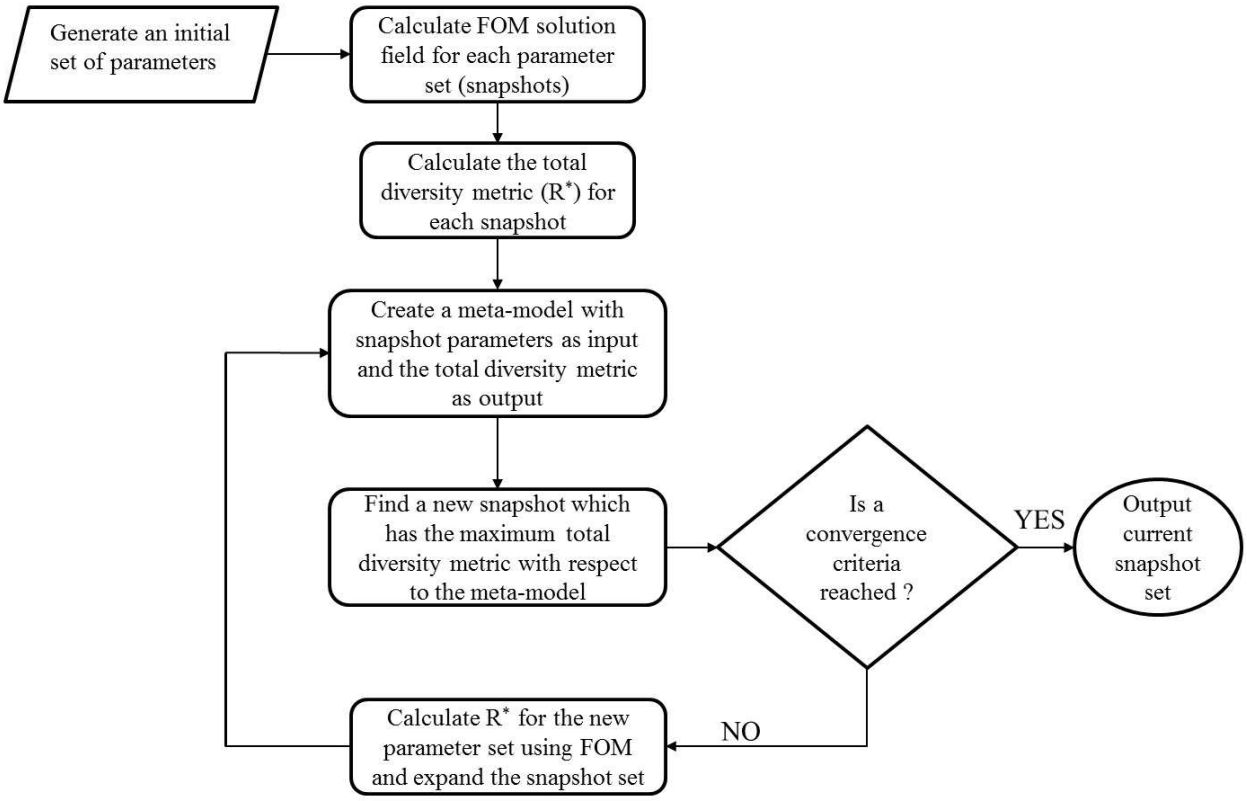

.

Figure 1.1: Flowchart describing the iterative snapshot generation algorithm.

of the snapshot sets, and the accuracy of these ROMs was quantified with respect to full-order analysis (i.e., traditional finite element analysis) and compared to the accuracy of similar POD ROMs created from randomly generated snapshot sets. Then, the iteratively generated ROM was incorporated into an inverse characterization solution procedure to show that the iteratively generated ROM can be created with a sufficient forward solution accuracy to allow for accurate and computationally efficient inverse solution processes.

1.4.1 Full-Order and Reduced-Order Forward Modeling

For both case studies it was assumed that the structures would be tested using frequency-response-based nondestructive testing (NDT) to then determine the material properties with nondestructive evaluation (NDE). Frequency-response-based NDT has proven diagnostic capability, and although displacement measurement is not particularly common, approaches have been developed to acquire such measurements [105, 101]. For the examples discussed here, the NDT consisted of a localized harmonic actuation applied normal to the surface of the structure at a given excitation frequency and the resulting steady-state harmonic vertical displacement amplitude was measured at a set of discrete sensor locations. Therefore, the physics for both examples was assumed to be described by steady-state dynamic solid mechanics, as described previously, and the full-order forward modeling was performed using the finite element method. The material behavior was assumed to be linear elastic with a homogeneous density and Poison's ratio of 2700 kg/m^3 and 0.3, respectively, and the semi-localized Young's modulus distribution was assumed to be defined with a radial basis function (RBF) as:

$$E(\vec{x}) = E_0 \left[1 - \alpha \cdot exp\left(-\frac{\left\| \vec{x} - \vec{\zeta} \right\|^2}{c} \right) \right], \tag{1.25}$$

where, $\|\cdot\|$ represents the l_2-norm, E_0 is the base Young's modulus, α is the percentage of the reduction in Young's modulus, $\vec{\zeta}$ is the center of the RBF, and c is the breadth of the RBF. In other words, each Young's modulus distribution considered was parametrized by four parameters, such that $\vec{\gamma} = [\alpha, \zeta_1, \zeta_2, c]^T$. For the specific examples herein, the base

Young's modulus was assumed to be known as a standard nominal value for aluminum, such that $E_0 = 69GPa$.

An important note is that for all examples the excitation frequency of the NDT was assumed to be a single fixed value (i.e., defined by the NDT), and therefore, only the parameters of the Young's modulus distribution were considered as variables to generate the ROMs. To apply the iterative snapshot generation approach to create the ROMs, the initial sets of snapshots were generated with full-order modeling based on uniformly distributed random values of the four unknown stiffness parameters (α, ζ_1, ζ_2, and c). Support vector regression [104, 44] was applied to create the surrogate models that would map the stiffness parameter values to R^* Eq. (1.22) based on the current set of snapshots at a given iteration of the iterative process. A genetic algorithm [39] was used to identify the new set of parameters that minimized R^* with respect to the surrogate model. The new parameter set was then simulated with the full-order model, the surrogate model was updated based on the expanded set of snapshots, and the process of iteratively generating the snapshots was repeated until the predefined (as stated for each example) maximum number of snapshots were generated. Finally, ROMs were created from the snapshot sets using the Galerkin weak form approach described in Section 2.2.

In the following examples, the forward modeling accuracy of the ROMs was first tested directly in comparison to the full-order modeling (i.e., the "gold standard" in terms of accuracy, but computationally inefficient) for several parameter sets that were not included in the snapshot sets, to directly quantify the generalization capabilities of the ROMs before considering an inverse characterization problem. To test the ROM accuracy a standard relative error metric was utilized for each parameter set as follows:

$$\text{Error}(\vec{\gamma}) = \frac{\|\vec{u}^{ROM}(\vec{x},\omega,\vec{\gamma}) - \vec{u}^{FOM}(\vec{x},\omega,\vec{\gamma})\|_\Omega}{\|\vec{u}^{FOM}(\vec{x},\omega,\vec{\gamma})\|_\Omega}, \tag{1.26}$$

where $\vec{u}^{ROM}$ and $\vec{u}^{FOM}$ are the displacement response fields calculated with the ROM and full-order model, respectively, and $\|\cdot\|_\Omega$ is the chosen norm over the spatial domain, Ω, with both the L_2 and L_∞ norms being considered in the following. To provide a baseline for comparing the accuracy of the iteratively generated ROMs, ROMs were also created for the

examples using an equivalent total number of randomly generated snapshots (generated in the same format as the initial set for the iterative approach).

1.4.2 Inverse Problem

To test the efficacy of the resulting ROMs to be used in a computational inverse problem solution procedure, each example case considered a corresponding set of tests in which the ROMs were used in an NDE procedure to estimate the stiffness parameters of the structures given simulated NDT measurements for several test cases. The simulated NDT for each case was assumed to produce harmonic displacement amplitudes measured at n_s discrete locations throughout the domain of the structures considered. Thus, in order to simulate NDT measurements, a set of material parameters were randomly selected and a full-order model was analyzed to produce displacement responses. For the second example, to add realism and avoid the inverse crime inherent in simulated experiments to some degree, Gaussian white noise was added to the displacement amplitude response at each measurement location.

Utilizing the ROMs, the inverse problem was cast as an optimization problem to determine the material parameters that minimize the relative difference between the simulated experimental NDT measurements and the response predicted by the ROM as:

$$\underset{\vec{\gamma}\in X}{\text{Minimize}} \quad \frac{\sum_{i=1}^{n_s}\left(\vec{u}^{ROM}(\vec{x_i},\omega,\vec{\gamma})-\vec{u}^{exp}(\vec{x_i},\omega)\right)^2}{\sum_{j=1}^{n_s}\left(\vec{u}^{exp}(\vec{x_j},\omega)\right)^2}, \tag{1.27}$$

where again X is the domain of the unknown stiffness parameters and $\vec{u}^{exp}$ is the simulated experimental displacement responses. A standard genetic algorithm was again applied to solve the above optimization problem and identify the parameters to estimate the Young's modulus distributions, and therefore, estimate the solution to the inverse problem. After optimization was completed, in addition to assessing the quality of the inverse characterization solutions, the measurement error for the final parameter estimates was recalculated substituting the full-order model response field generated with the final parameter estimates in place of the ROM response field in the objective functional in Eq. (1.27). In other words, the results were tested to examine whether the error level achieved by using the ROM during

the optimization process was comparable to the error that could have been obtained by the full-order model instead (albeit, with much more computational expense). The quality of the final inverse problem solution estimates were quantified through the relative L_2-error between the Young's modulus distribution defined by the parameters used to create the simulated experimental data and that estimated by the inverse characterization results as:

$$\frac{\left(\int_\Omega \left(E(\vec{x},\vec{\gamma}^{exp}) - E(\vec{x},\vec{\gamma}^{inv})\right)^2 d\vec{x}\right)^{1/2}}{\left(\int_\Omega \left(E(\vec{x},\vec{\gamma}^{exp})\right)^2 d\vec{x}\right)^{1/2}}, \tag{1.28}$$

where $\vec{\gamma}^{exp}$ are the parameters used to create the simulated experimental measurement data and $\vec{\gamma}^{inv}$ are the corresponding inverse solution estimates.

1.4.3 Example 1 - Plate

The first case study consisted of a $1m \times 1m \times 0.02m$ aluminum plate subject to a $1kPa$ harmonic load applied to a $5cm$ region normal to the top surface of the plate, excited to steady-state with an actuation frequency of $400Hz$. The plate was assumed to be fixed along the bottom boundary and free to displace along the other three boundaries. Fig. **??** shows the schematic of this first test case and the sensor locations, which were uniformly distributed in each row, that were used for the NDE portion of the study.

For the iterative snapshot generation approach, an initial random set of 10 snapshots was generated, and then the iterative surrogate modeling approach was iteratively applied to generate the remaining snapshots in the set used to create the ROM. To examine the dependence on the total number of snapshots, snapshot sets of 10 (i.e., the original randomly generated set), 20, 30, 40, 50, and 60 were investigated, in turn. In addition, as noted previously, snapshot sets of the equivalent total size were completely randomly generated (i.e., no iteratively generated snapshots) for comparison purposes. In order to test the accuracy of each ROM, 100 parameter sets were randomly generated and the relative error between the ROM and the FOM responses Eq. (1.26) was calculated for each parameter set.

Figure **??** shows the average and standard deviation of the relative ROM error for the 100 test cases for both the iteratively generated ROMs and the randomly generated ROMs.

As would be expected, for both approaches, the average error as well as the standard deviation of the error for the resulting ROM decreased as the number of snapshots used to construct the ROM increased. More interestingly, the ROM error corresponding to the iteratively generated snapshots was substantially lower than the the ROM error corresponding to the randomly generated snapshots by approximately a factor of 2 or more for every size of the snapshot set. In addition, the standard deviation of the error for the iteratively generated ROMs decreased considerably more quickly than the randomly generated ROMs, and while the iteratively generated ROMs appeared to have a distinguishable better performance in terms of decreasing $L_2 - Error$ at 50 snapshots, the randomly generated ROMs show no such signs of performance.

To assess the capabilities to use the iteratively generated ROMs to approximate the solution to an inverse problem, the iteratively generated ROMs were used to inversely approximate semi-localized Young's modulus distributions, as described by Eq. (1.25), based on the NDT and inverse solution procedure described above. In particular for this example, the inverse solution process was tested with five different randomly generated material distributions (i.e., damage scenarios), and each scenario was approximated using the iteratively generated ROMs constructed with 20, 40, and 60 total snapshots, in turn. The stopping criteria for the genetic algorithm optimization for each trial was set to be a maximum of 2000 ROM evaluations.

Table 1.1 shows the material parameters used to create the simulated experimental measurement data for the five scenarios considered and the corresponding parameters estimated by the inverse solution process with the various ROMs (built from 20, 40, and 60 total snapshots), the respective ROM measurement error for the inverse solutions (as defined by Eq. (1.27)), the respective FOM measurement error for the inverse solutions (substituting the FOM in place of the ROM in Eq. (1.27)), and the error in the respective Young's modulus distributions predicted by the inverse solution estimates (as defined by Eq. (1.28)).

In addition, to provide further perspective on the relative accuracy of the Young's modulus distributions obtained by the inverse solution process, Figure 1.2 shows (as a representative example) the target (i.e., simulated experimental) Young's modulus distribution for the fourth scenario compared to the Young's modulus distribution that was inversely estimated

Table 1.1: Target (i.e., simulated experimental) values for the RBF amplitude (α), the breadth of the RBF (c_1), and the coordinate of the center of the RBF (ζ_1, ζ_2) defining the Young's modulus distribution, the corresponding parameters estimated with the inverse characterization process using the ROMs created with 20 (ROM-20), 40 (ROM-40), and 60 (ROM-60) iteratively generated snapshots, and the respective ROM measurement error (M_E), the FOM measurement error (F_E), and the error in the predicted Young's modulus distribution (Y_E) for the five test cases (i.e., damage scenarios) for Example 1 - Plate.

Test #	Method	α	ζ_1	ζ_2	c	$M_E(\%)$	$F_E(\%)$	$Y_E(\%)$
	Target	0.701	0.592	0.511	0.004			
	ROM-20	0.544	0.652	0.481	0.003	2.78	3.45	0.37
1	ROM-40	0.552	0.610	0.536	0.005	1.53	1.86	0.01
	ROM-60	0.552	0.607	0.521	0.005	1.45	1.57	0.01
	Target	0.416	0.841	0.832	0.002			
	ROM-20	0.310	0.763	0.782	0.003	0.72	3.12	0.04
2	ROM-40	0.384	0.803	0.791	0.002	0.52	2.73	0.02
	ROM-60	0.405	0.824	0.801	0.002	0.49	1.67	0.07
	Target	0.540	0.869	0.264	0.003			
	ROM-20	0.407	0.781	0.396	0.005	5.61	4.82	0.32
3	ROM-40	0.601	0.855	0.202	0.001	3.52	2.67	0.13
	ROM-60	0.451	0.860	0.236	0.003	1.46	2.22	0.08
	Target	0.639	0.544	0.647	0.005			
	ROM-20	0.558	0.598	0.607	0.003	2.89	5.14	0.48
4	ROM-40	0.583	0.576	0.683	0.004	2.4	2.39	0.27
	ROM-60	0.608	0.532	0.651	0.004	2.11	1.5	0.24
	Target	0.066	0.404	0.448	0.007			
	ROM-20	0.048	0.488	0.337	0.005	0.65	4.93	0.07
5	ROM-40	0.071	0.381	0.411	0.005	0.48	3.01	0.03
	ROM-60	0.061	0.414	0.491	0.006	0.46	2.47	0.03

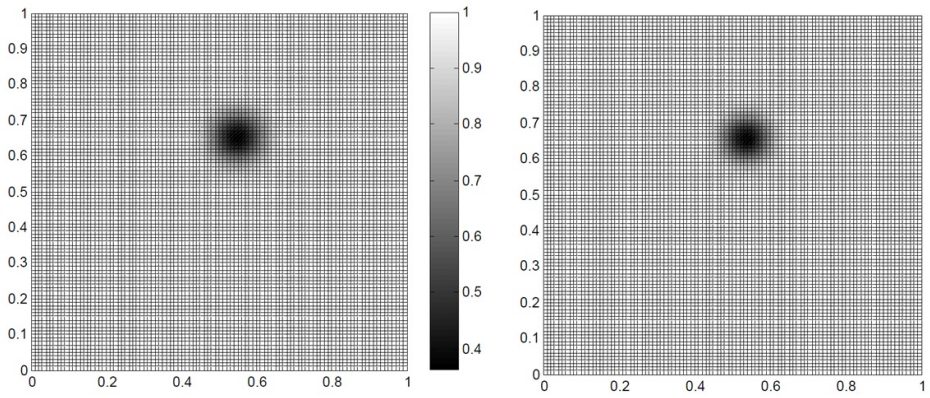

Figure 1.2: Spatial distribution of the Young's modulus from (a) the target (simulated experiment) and (b) the inverse characterization estimate with the ROM built from 60 iteratively generated snapshots for the fourth test scenario for Example 1 - Plate.

using the ROM built from 60 iteratively generated snapshots. Overall, the optimization process was able to sufficiently match the ROM response to the measurement data, with only one scenario (the third scenario) having a ROM measurement error in excess of 5%. Thus, the iteratively generated ROMs were able to at least produce response estimates that relatively accurately matched the measurement data. More importantly, the FOM responses with the inverse solution estimates also sufficiently matched the measurement data, even though the optimization was performed with the ROM. Moreover, the FOM measurement error was minimally higher than the ROM measurement error, again with only one scenario (the fourth scenario for the FOM) having a FOM measurement error in excess of 5%. In other words, the inverse problem solution estimates obtained with the ROMs were nearly as accurate with respect to the FOM in terms of the measurement data, and were still within an error range in terms of the FOM to be considered an inverse problem solution estimate. As would be expected, corresponding to the accuracy in the measurement error, the resulting estimates of the Young's modulus distributions were accurate for all five scenarios and all three ROMs, with Young's modulus reconstruction errors of less than 1% for every test. There

was a noticeable reduction in accuracy (in terms of the achievable measurement errors and the Young's modulus reconstruction) for the ROMs generated with 20 snapshots compared to 40 and 60, which is not surprising considering the forward modeling accuracy shown in Figure **??**. However, even for the lowest-accuracy case of 20 snapshots, the inverse solution process was able to be sufficiently applied to produce accurate inverse solution estimates with the iteratively generated ROMs.

1.4.4 Example 2 - Airfoil

To examine a substantially more realistic and computationally expensive example, the second simulated case study consisted of analysis of an aluminum airfoil structure based upon the standard NACA-0012 cross section, shown schematically in Figure (**??**). The test consisted of $1kPa$ harmonic loads applied simultaneously to two circular regions with $2cm$ radii normal to the top surface of the airfoil, and the airfoil was excited to steady-state with an actuation frequency of $400Hz$. The airfoil was fixed on one side and free to displace along all of the remaining boundaries. In order to slightly simplify the problem, the semi-localized change in the Young's modulus distribution was assumed to only occur in the upper portion of the airfoil and the modulus value was kept constant through the thickness of the airfoil. Therefore, the two-dimensional parameterization of the Young's modulus described by Eq. (1.25) was still applicable as the description of the in-plane Young's modulus distribution of the top half of the airfoil. A similar distribution of sensors was used for the NDE portion of this second study as was used in the first example. The sensors were assumed to measure the vertical displacement and the sensor layout is also shown in Figure (**??**).

The same iterative snapshot generation procedure was repeated as was used for the first example, starting with 10 snapshots and then iteratively generating the remaining snapshots for the sets to create the ROMs. Again, total snapshot sets of 20, 30, 40, 50, and 60 were generated and analyzed, and equivalent sets of entirely randomly generated snapshots were created for comparison. 100 new parameter sets were randomly generated and the relative error Eq. (1.26) between the ROM and the FOM responses Eq. (1.26) was calculated for each new parameter set.

Figure 1.3 shows the average and standard deviation of the relative ROM error for the 100 airfoil test cases for both the iteratively generated and randomly generated ROMs. Although the error levels were considerably higher (approximately doubled) for this second (more complex) example, the reduction in the error as the number of snapshots increased and the substantially lower error for the iteratively generated ROMs compared to the randomly generated ROMs (by approximately a factor of 2 or more again) were nearly identical to the first example. One noticeable difference between this example and the previous is that the error level for the iteratively generated ROMs did not tend to be converged as it did for the first example.

The capabilities to use the iteratively generated ROMs within an inverse solution procedure, as described above, was again examined for this airfoil example. As mentioned previously, to add additional realism for this second example, 1% Gaussian white noise was added to the simulated NDT displacement measurements for each sensor prior to applying the inverse characterization procedure, such that:

$$\vec{u}^{exp}(\vec{x},\omega) = \vec{u}^{FOM}(\vec{x},\omega,\vec{\gamma}^{exp}) \cdot (1 + 0.01\aleph), \tag{1.29}$$

where $\aleph$ is a normally distributed random variable with zero mean and unit variance. For this second example only two different randomly generated material distributions (i.e., damage scenarios) were considered. However, to examine the consistency of the inverse solution procedure with the ROM, particularly considering the stochastic nature of the inverse solution process described, the inverse characterization process was repeated 10 times for each test case. Only the most accurate ROM (i.e., the ROM created from 60 iteratively generated snapshots) was utilized for the inverse solution procedure and the stopping criteria for the genetic algorithm optimization for each trial was set to be a maximum of 5000 ROM evaluations.

Table 1.2 shows the material parameters used to create the two sets of simulated experimental measurement data and the corresponding parameters estimated by the inverse solution process with the ROM built from 60 iteratively generated snapshots, the respective ROM measurement error for the inverse solutions (as defined by Eq. (1.27)), the respective FOM measurement error for the inverse solutions (substituting the FOM in place of

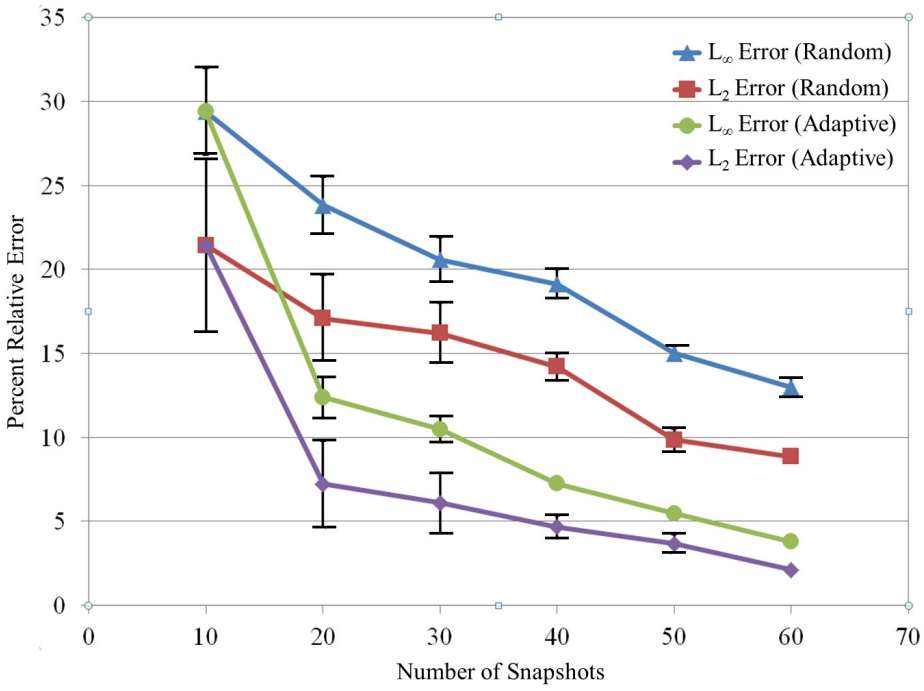

Figure 1.3: Average and standard deviation (error bars) with respect to the 100 test cases of the relative L_2 and L_∞ ROM errors for the randomly generated (Random) and the iteratively generated (Iterative) ROMs for Example 2 - Airfoil.

the ROM in Eq. (1.27)), and the error in the respective Young's modulus distributions predicted by the inverse solution estimates (as defined by Eq. (1.28)). To again provide a representative example for perspective on the relative accuracy of the Young's modulus distributions obtained by the inverse solution process, Figure 1.4 shows the target Young's modulus distribution for the second scenario compared to the inversely estimated Young's modulus distribution. Similar to the first example, the optimization solution process was successful in minimizing the measurement error with respect to the ROM in all trials, as can be seen from the average ROM measurement error that was even lower than the first example cases and an almost negligible standard deviation of that error. The FOM measurement error was again higher than the ROM measurement error, but also consistently a more than sufficiently low value to consider the inverse solution estimate to be legitimate. Thus, all 20 solutions (10 solution trials for each of the 2 scenarios) produced nearly exact (with a solution error less than 1%) estimate of the Young's modulus, even in the presence of measurement noise. What is particularly significant is that computing cost (i.e., CPU time) of each ROM was only 0.8 *seconds* compared to the 63 *seconds* for the FOM. In other words, the iteratively generated ROM was able to be consistently used to produce accurate inverse solution estimates in approximately 1 *hour* of computing time, while the FOM would have required 88 *hours* of computing time to produce equivalent estimates.

1.5 CONCLUSION

An approach was presented to efficiently create reduced-order models based on the Galerkin weak-from approach for computational mechanics that are optimally accurate over a range of system input parameters. The core component of the approach was the algorithm presented for iteratively generating the ensemble of full-order model response fields used to create the ROM to maximize the overall diversity of the ensemble, and thereby, improve the accuracy of the resulting ROM. Although shown in the context of steady-state dynamic solid mechanics, the approach is generally applicable to a broad range of physical processes and applications. Through two case studies of harmonically excited structural components the iterative ap-

Table 1.2: Target (i.e., simulated experimental) values for the RBF amplitude (α), the breadth of the RBF (c_1), and the horizontal and vertical locations of the center of the RBF (ζ_1, ζ_2) defining the Young's modulus distribution, the mean and standard deviation (from the 10 repetitions) of the corresponding parameters estimated with the inverse characterization process using the ROM created with 60 iteratively generated snapshots (ROM-60), the respective ROM measurement error (M_E), FOM measurement error (F_E), and error in the predicted Young's modulus distribution (Y_E) for the two test cases (i.e., damage scenarios) for Example 2 - Airfoil.

Test #	Method	α	ζ_1	ζ_2	c	$M_E(\%)$	$F_E(\%)$	$Y_E(\%)$
1	Target Value	0.927	0.192	0.138	0.006			
	ROM-60							
	Mean	0.884	0.127	0.105	0.005	0.63	1.82	0.39
	Std. Dev.	0.117	0.024	0.018	0.001	0.07	0.17	0.03
2	Target Value	0.093	0.525	0.861	0.004			
	ROM-60							
	Mean	0.090	0.491	0.895	0.004	0.49	1.37	0.06
	Std. Dev.	0.004	0.051	0.090	0.001	0.05	0.15	0.01

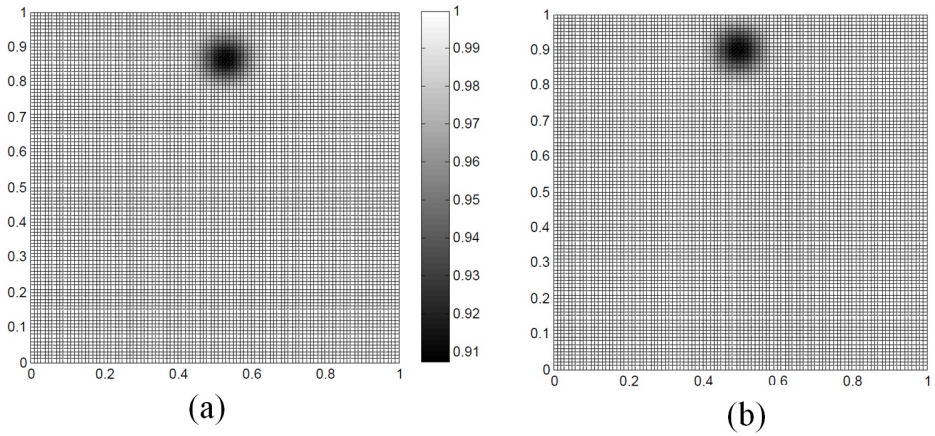

Figure 1.4: Spatial distribution of the Young's modulus from (a) the target (simulated experiment) and (b) the inverse characterization estimate with the ROM built from 60 iteratively generated snapshots for the second test scenario for Example 2 - Airfoil.

proach was shown to produce ROMs that could accurately estimate the system response over a wide range of input material parameters, particularly in comparison to ROMs built from randomly generated ensembles of FOM response fields. Moreover, the iterative approach was shown to produce ROMs with sufficient accuracy and generalization over the range of input system parameters to facilitate computationally inexpensive and consistently accurate inverse characterization of material properties through a series of simulated nondestructive evaluation problems.

2.0 EVALUATION OF POD-BASED MODEL REDUCTION STRATEGIES TOWARD EFFICIENT SIMULATION OF TURBULENT FLOWS PAST BLUFF BODIES

2.1 ABSTRACT

A numerical investigation is presented regarding the efficiency and accuracy of a set of contemporary proper orthogonal decomposition (POD) based reduced-order modeling (ROM) approaches for capturing the behavior of turbulent flows past bluff bodies. In particular, this investigation seeks to evaluate the potential of the ROM approaches to predict not only the variation in time of such flow systems, but also changes in the system response due to changes in other input parameters, such as the system Reynolds (Re) number, while maintaining a substantial reduction in computational cost compared to traditional computational fluid dynamics (e.g., finite volume). Two fundamentally different ROM approaches that similarly utilize a POD basis are evaluated and compared: (1) the Galerkin projection approach, in which the Navier-Stokes equations are projected onto the low dimensional POD basis, and (2) a surrogate modeling approach in which the governing equations of the system are replaced with a surrogate mapping (e.g., radial basis function interpolation/extrapolation) of the modal coefficients of the POD basis. These two ROM strategies are compared through a set of numerical case studies for flow past a single cylinder as well as flow past a cluster of four cylinders, both for a range of time and Re number variations. For all tests a standard Unsteady Reynolds-Averaged Navier-Stokes (URANS) method was used both for generating the fluid velocity field datasets needed to create a POD basis and to compare with for evaluating the ROM accuracies. For predicting responses in time with a fixed Re number for a single cylinder, all of the ROMs were relatively accurate, but the surrogate model ROMs

were significantly more accurate than the Galerkin projection ROMs, particularly at the lower values of Re number. Alternatively, for predicting the flow response for varying Re number, the surrogate model approach became ineffectual (errors greater than 100%), while the Galerkin projection approach increased in error by a relatively small amount compared to prediction with fixed Re number. For the example of flow past a cluster of four cylinders, the accuracy of both ROM approaches was commensurate for predicting responses in time with fixed Re number (i.e., the accuracy of the surrogate model approach decreased significantly), and the maximum error of the ROM approaches increased by only a relatively small amount compared to the single cylinder example. As before, the surrogate model approach was unable to accurately predict variations in Re number, while the Galerkin projection approach was approximately as accurate as for the single cylinder example.

2.2 INTRODUCTION

Despite improvements in computing power and progress of computational fluid dynamics (CFD), the numerical solution of Navier-Stokes (NS) equations to describe the behavior of a flow is still prohibitive for many applications. For example, CFD solvers often require hundreds of thousands of degrees of freedom to accurately capture flow fields even of relatively simple systems. For optimization problems, which require obtaining several solution fields, or for feedback control problems for which real-time solutions are needed, it is not often feasible to utilize traditional CFD solvers. Hence, some form of accurate and realistic model reduction is necessary for enabling computational analysis to aid in a variety of engineering applications [88],[16]. One example application that requires model reduction is simulating flow within nuclear reactor components [26]. For example, Figure 2.1 shows a schematic of a conceptual very high temperature reactor (VHTR) lower plenum. In this complex mixing flow, anywhere from 50 to 100 fluid jets, with large inlet velocities (100 m/s) and large spreads in temperatures (100°C), turn 90 degrees and merge to create a cross-flow that negotiates a bank of cylindrical supports. Simulating such a complicated thermo-fluid system with turbulent mixing would likely be computationally infeasible with standard (i.e., full-order)

CFD solvers. Moreover, even simulating components of such a system such as turbulent flow over one or more cylinders can be computationally burdensome. There are a variety of approaches that have been developed for model reduction for a wide range of applications involving fluid mechanics [99], [24]. The particular focus herein is on those reduced-order modeling strategies that seek to derive a relatively low-dimensional basis to represent the response of the system of interest from an ensemble of possible response fields that have been acquired a priori (often from a relatively small number of full-order analyses). Different methods have been applied to process an ensemble of data to produce reduced-order bases, including balanced truncation [42], Krylov subspaces [10], Proper Orthogonal Decomposition (POD), and balanced POD [94]. Due to its optimality in the sense of minimizing the average L2 error and convergence properties, the POD method is used in the present work to obtain reduced-order bases. Furthermore, POD has been used in numerous applications to create ROMs of fluid flows, including forward modeling of fluid dynamics [93], [54] as well as optimal control applications [95].

One aspect that is clearly important when creating a reduced-order model (ROM) is generating a basis that is in some sense a good representation of the system considered under any conceivable system variation. For example, in a fluid dynamics application a ROM may need to be capable of capturing the flow behavior accurately not only for changes in time or frequency, but also for changes in Re number. One approach to such ROM generalization is the Generalized POD (GPOD) method [106], [100], which attempts to make a sufficiently diverse initial dataset through sampling the potentially variable system parameters (e.g., time/frequency, material properties, Reynolds number, etc.) and generating response fields with full-order models with those parameters such that the basis acquired is applicable to all possible system variations. Alternatively, other approaches that have been developed attempt to somehow manipulate the basis to be used in a ROM for a given set of system parameters (i.e., to make the basis a function of the input parameters), such as the Interpolation of Reduced Basis Vector method [28] and the Subgrid Angle Interpolation Method [68], [66], [67]. The present work utilizes a GPOD approach, based on the simplicity of the implementation and the fact that the ROM built using the GPOD approach can be used for

any set of system parameters desired without any need for updating (as would be the case for the other approaches mentioned).

More importantly to the present work, once the low-dimensional basis is derived, there are different approaches to utilizing these bases in order to produce a ROM. These approaches can be divided into two categories: (1) those that project the low-dimensional basis onto the original governing equations of the system (e.g., NS equations) and (2) those that instead integrate the basis into a surrogate model (e.g., regression-based) strategy. An example of the first strategy is the standard Galerkin projection (i.e., weighted integral) of the basis onto the NS equations, which has been previously applied to several fluid dynamics problems, such as simulation of shear layers [87], flow around an airfoil [61], cavity flow [20], and flow past a cylinder [27], [64]. Similarly, surrogate modeling approaches have also been previously applied in the context of fluid dynamics, including [108] that presented a number of surrogate modeling approaches for aerodynamic simulation and [80] that used radial basis function regression for approximating the 3D Lorenz model as well as turbulent flow, among others. Generally, these two ROM approaches have a tradeoff between accuracy and computational efficiency. Projection approaches are typically more accurate, as they include the physics-derived governing equations of the system in comparison to surrogate modeling approaches, but are considerably more computational expensive as they still require numerical integration over the system domain and potentially the solution of an ordinary differential equation (if the system is transient).

Towards understanding the potential capability of ROM strategies to capture the complex behavior of turbulent flows that may occur within nuclear reactor components (such as the lower plenum shown in Figure 2.1), the present work focuses on the benchmark example of isothermal flow past one or more cylinders. The example of flow past a cylinder was chosen as it has a simple geometry, coherent structures (i.e., basis functions obtained by POD) can be captured easily, and the behavior involves both vortex shedding phenomenon and separated flow [112]. Previous studies have similarly investigated physics-based ROM for flow past bluff bodies. The work in [81] introduced the concept of a shift-mode representing the mean-field correction, which was shown to describe the Reynolds-number dependence of a flow with reasonable accuracy. Galletti et al. [37] studied the validity of POD-ROM of a laminar

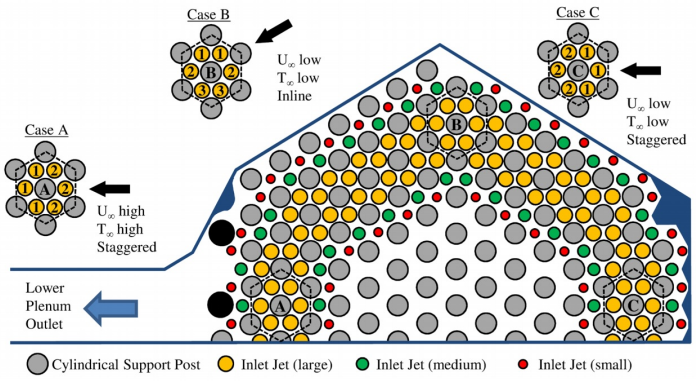

Figure 2.1: Lower plenum geometry including support posts and inlet jets [77]

flow past a square cylinder for Reynolds numbers that are different from those for which the model was derived, and showed that the long-term dynamics can be accurately captured with some variations of the Reynolds number. Siegen et al. [102] proposed a double proper orthogonal decomposition (DPOD) approach to capture the evolution of the limit cycles for flow past a single cylinder in the laminar regime. Alternatively, the focus of the present study is on comparing and contrasting the capabilities of two ROM strategies: (1) a Galerkin projection approach and (2) a surrogate modeling approach for ROM of turbulent flows past cylinders. In addition, the present work examines the effectiveness of these ROM strategies with respect to predicting in time and with variations in Reynolds number, as well as for increasing the system complexity with the inclusion of more than one cylinder in the flow field.

The following section details the POD reduced-order modeling methods utilized herein, including the Galerkin projection approach and the surrogate modeling approach (i.e., surrogate model approach). Then, the ROM approaches are evaluated and compared numerically through a set of flow past cylinder(s) example problems in Section 2.4, which is followed by concluding remarks in Section 2.5.

2.3 POD REDUCED-OREDER MODELING OF INCOMPRESSIBLE NS EQUATIONS

The core hypothesis of any POD-ROM approach is that a relatively small number of full-order (i.e., traditional CFD solvers) analyses based upon different values of the input parameters of interest (Re number or time levels herein) contain fundamental information about the potential solution fields of the Boundary Value Problem (BVP) and can be used to derive a low-dimensional basis that can predict the solution fields for a range of input parameters (not just the specific parameter values used to generate the set of full-order analyses) without substantially less accuracy compared to the full-order model. The problem of determining the POD basis can be cast as an optimization problem to determine the set of m modes $\{\phi_i(\vec{x})\}_{i=1}^{m}$ given a set of n full-order analysis fields (where generally m is much smaller than n) $\{u(\vec{x},\vec{\gamma}_k)\}_{k=1}^{n}$, for each variation of the input parameters of interest $\vec{\gamma}_k$, such that the average L_2 error between full-order analysis and its projection on the subspace is minimized. Through several manipulations, including applying the method of snapshots [103], the POD optimization problem can be transformed into the following n-dimensional eigenvalue problem:

$$\frac{1}{n}\sum_{k=1}^{n} A_{jk}C_k = \lambda C_j, \tag{2.1}$$

where

$$A_{jk} = \int_{\Omega} \vec{u}(\vec{x},\vec{\gamma}_j)\cdot\vec{u}(\vec{x},\vec{\gamma}_k)d\vec{x}. \tag{2.2}$$

An optimal set of as many as n orthogonal basis functions (i.e., POD modes) can then be determined by:

$$\vec{\phi}_i(\vec{x}) = \frac{1}{\lambda^{(i)}n}\sum_{k=1}^{n}\vec{u}(\vec{x},\vec{\gamma}_k)C_k^{(i)}, \quad \text{for } i = 1,2,...,n, \tag{2.3}$$

where $C_k^{(i)}$ is the k^{th} component of the i^{th} eigenvector from the solution of equation 2.1 and $\lambda^{(i)}$ is the corresponding eigenvalue. $\lambda^{(i)}$ is often considered a measure of the usefulness of the corresponding mode $\vec{\phi}_i(\vec{x})$ for approximating the given dataset of potential solution fields. Therefore, a common procedure (as was done herein) is to only use the m modes with the highest corresponding eigenvalues, with $m<n$, for any subsequent solution approximation,

and the remaining modes are discarded (In the present work the set with corresponding eigenvalues that represent approximately 99% of the total sum of the n eigenvalues is used). The percentage of kinetic energy that each mode contains can be calculated as follows:

$$E(i) = \frac{\lambda^{(i)}}{\sum_{i=1}^{n} \lambda^{(i)}} \tag{2.4}$$

2.3.1 POD-Galerkin Projection Approach for Reduced-Order Modeling

Once the POD modes are obtained, the NS equations can be projected onto these modes through a standard Galerkin procedure [90]. The incompressible NS equations can be shown as:

$$\rho(\frac{\partial}{\partial t}\vec{u}(\vec{x},t) + \vec{u}(\vec{x},t)\cdot\nabla\vec{u}(\vec{x},t)) = -\nabla p(\vec{x},t) + \mu\nabla^2\vec{u}(\vec{x},t) \tag{2.5}$$

$$\rho\nabla\cdot\vec{u}(\vec{x},t) = 0, \tag{2.6}$$

where ρ is the fluid density which is assumed to be constant, and, μ is the fluid viscosity which is also assumed to be constant. The weak form (see for example [90]) of Equations 2.5 and 2.6 can be derived by taking the inner product of Equation 2.5 with test functions which satisfy $\vec{v} \in L^2(\Omega)$, where, $L^2(\Omega)$ is a set of functions that are square-integrable along with their first derivative in the domain Ω. Then, integrating over the domain, the weak form of the BVP can be written as:

$$\int_\Omega \rho\vec{v}(\vec{x})\cdot\frac{\partial}{\partial t}\vec{u}(\vec{x},t)d\vec{x} + \int_\Omega \rho\vec{v}(\vec{x})\vec{u}(\vec{x},t)\nabla\cdot\vec{u}(\vec{x},t)d\vec{x} - \int_\Omega p\nabla\cdot\vec{v}(\vec{x})d\vec{x} + \int_\Omega \mu\nabla\cdot\vec{v}(\vec{x})\nabla\cdot\vec{u}(\vec{x},t)d\vec{x} = 0. \tag{2.7}$$

To implement the POD modes into the above weak form to create a ROM all that is then necessary is to apply the m previously obtained vector modes, $\{\phi_{ji}\}_{j=1}^{m}$, as the test and trial functions such that:

$$\vec{v}(\vec{x}) = \vec{\phi}_q(\vec{x}), \quad \text{for} \quad q = 1, 2, ..., m, \tag{2.8}$$

and

$$\vec{u}(\vec{x},t) = \vec{\bar{u}}(\vec{x}) + \sum_{r=1}^{m} a_r(t)\vec{\phi}_r(\vec{x}), \tag{2.9}$$

where $\bar{\vec{u}}(\vec{x})$ is the average velocity field calculated from the ensemble used to generate the modes and a_r is the modal coefficient corresponding to the r^{th} POD mode (i.e., the coefficients to be solved for in the ROM velocity numerical approximation). Noting that if the modes are generated from an ensemble that assumes incompressibility (as is the case herein), then the modes will be divergence-free. Substituting Equation **??** and Equation 2.8 into Equation 2.7 results in the following equation:

$$\int_\Omega \rho\vec{\phi}_q(\vec{x})(\frac{\partial}{\partial t}\vec{u}(\vec{x},t)+\vec{u}(\vec{x},t)\nabla\cdot\vec{u}(\vec{x},t))+\mu\nabla\cdot\vec{\phi}_q(\vec{x})\nabla\cdot\vec{u}(\vec{x},t)d\vec{x}-\int_\Gamma p(\vec{x},t)\vec{\phi}_q(\vec{x})\cdot\vec{n}(\vec{x})d\vec{x}=0, \tag{2.10}$$

where $\vec{n}(\vec{x})$ represents the normal vector to each boundary.

The second integral in Equation 2.10, which is over the boundaries, requires careful consideration since it involves the pressure term. As long as the POD modes are symmetric, so that the inlet fluxes and the outlet fluxes cancel with each other, the second integral in Equation 2.10 can be eliminated. In the present work, as will be explained later, the POD modes are symmetric, and therefore the aforementioned integral can be eliminated.

Substituting the solution expansion (Equation 2.9) into Equation 2.10, a non-linear evolution equation for the coefficients can be obtained as:

$$\rho\dot{a}_q+\sum_{s=1}^{m}\sum_{r=1}^{m}(A_{qrs}a_ra_s+B_{qr}a_r)+C_q=0,\quad \text{for}\quad q=1,2,...,m, \tag{2.11}$$

where

$$A_{qrs}=\int_\Omega\vec{\phi}_q(\vec{x})\cdot(\vec{\phi}_r(\vec{x})\cdot\nabla)\vec{\phi}_s(\vec{x})d\vec{x}, \tag{2.12}$$

$$B_{qr}=\int_\Omega\vec{\phi}_q(\vec{x})\cdot(\vec{u}_m(\vec{x})\cdot\nabla)\vec{\phi}_r(\vec{x})d\vec{x}+\vec{\phi}_q(\vec{x})\cdot(\vec{\phi}_r(\vec{x})\cdot\nabla)\vec{u}_m(\vec{x})d\vec{x}+\int_\Omega\nabla\cdot\vec{\phi}_q(\vec{x})\nabla\cdot\vec{\phi}_r(\vec{x})d\vec{x}, \tag{2.13}$$

and

$$C_q=\int_\Omega\vec{\phi}_q(\vec{x})\cdot(\vec{\bar{u}}_m(\vec{x})\cdot\nabla)\vec{u}_m(\vec{x})d\vec{x}+\int_\Omega\nabla\cdot\vec{\phi}_q(\vec{x})\nabla\cdot\vec{u}d\vec{x}. \tag{2.14}$$

The initial condition for Equation 2.11 is as follows:

$$a_q|_{t=0}=\int_\Omega\vec{\phi}_q(\vec{x})\ \cdot\vec{u}(\vec{x},t)|_{t=0}\ d\vec{x}. \tag{2.15}$$

Equation 2.11 can be solved with any standard nonlinear ordinary differential equation solution method to determine the values of each modal coefficient over the time domain of the problem considered, $a_q(t)$, and thereby approximate the flow field through a ROM.

2.3.2 Surrogate Model Approaches

Surrogate model approaches are relatively more straightforward and computationally inexpensive in comparison to the POD-Galerkin approach. The use of a surrogate model approach with POD for prediction of new solution fields requires the transformation of modal coefficients, a_i, from the discrete sample space for which they have been computed to a continuous space through some form of regression. If it is assumed that a_i varies as a smooth function with the change in system parameters, then a surrogate model may be used to determine the modal coefficients at intermediate parametric values not included in the original data ensemble.

The first step in surrogate model approaches is snapshot reconstruction. Each snapshot can be reconstructed using the obtained POD modes based on the following equation:

$$\vec{u}(\vec{x},\vec{\gamma}_q) - \vec{\bar{u}}(\vec{x}) = \sum_{j=1}^{N} \hat{\alpha}_j(\vec{\gamma}_q)\,\vec{\phi_j}(\vec{x}) \quad \text{for} \quad q = 1, 2, ..., n \tag{2.16}$$

where, $\hat{\alpha}_j(\vec{\gamma}_q)$ is the modal coefficient for the q^{th} velocity field with the j^{th} mode, which can be obtained from the following:

$$\hat{\alpha}_j(\vec{\gamma}_q) = \int_{\Omega} \vec{\phi_q}(\vec{x})(\vec{u}(\vec{x},\vec{\gamma}_q) - \vec{\bar{u}}(\vec{x}))\; d\vec{x}. \tag{2.17}$$

Then, some method for interpolating/extrapolating these modal coefficients is applied, with two options considered herein: radial basis functions (RBF) and Kriging. The RBF approach constructs a linear space from which the interpolation functions are chosen dependent upon the position of the data points in the parameter space. The RBF formulates this dependency as a linear combination of functions with radial symmetry about each parameter set as:

$$\hat{\alpha}_j(\vec{\gamma}) = \sum_{i=1}^{n} \zeta_i \varphi(||\vec{\gamma} - \vec{\gamma}_i||), \tag{2.18}$$

where ζ_i is the i^{th} weighting coefficient (to be determined by regression), the norm is the Euclidean norm, and φ is the chosen RBF. Various options are available for the form of the function φ such as linear, cubic, Gaussian, etc [50]. Similar to the work done by Gunes [43],

for Kriging approach, this study employed the DACE method [71]. The form of the Kriging interpolation function is:

$$\hat{\alpha}_j(\vec{\gamma}) = \sum_{i=1}^{n} \zeta_i \exp\left(-\sum_{j=1}^{d} \vartheta ||\vec{\gamma} - \vec{\gamma}_i||^{p_j}\right), \tag{2.19}$$

where ζ_i is again the i^{th} weighting coefficient and p_j is an additional coefficient to be determined by regression, the norm is again the Euclidean norm, and ϑ is the Kriging function (see [71] for additional details). Once the chosen surrogate model approximation of the modal coefficients has been created, any new velocity field can be predicted simply using:

$$\vec{u}(\vec{x}, \vec{\gamma}) = \vec{\bar{u}}(\vec{x}) + \sum_{i=1}^{m} \hat{\alpha}_j(\vec{\gamma}) \phi_{ij}(\vec{x}). \tag{2.20}$$

2.4 EXAMPLES

To evaluate and contrast the ROM approaches described (both Galerkin projection and surrogate modeling), a set of numerical case studies was performed consisting of turbulent flow past a single cylinder as well as turbulent flow past a cluster of multiple cylinders. Table 2.1 lists all Re numbers considered for both examples and the corresponding inlet velocities. For all test cases, standard Unsteady Reynolds Averaged Navier-Stokes (URANS) [35] simulations were used to acquire the ensembles of velocity solution fields (i.e., snapshot sets) to use to generate the POD modes. As an example, Table 2.1 also provides the resulting vortex shedding periods and the Strouhal numbers produced by this URANS full-order modeling of each Re number for flow past a single cylinder, which was used to confirm the accuracy of these solutions.

The time sampling to generate the snapshot sets was performed such that the velocity fields were acquired at 15 uniformly spaced time points within one complete vortex shedding period for each Re number. The vortex shedding periods were characterized by the time history of the simulated lift coefficients, such as the example for flow past a single cylinder

Table 2.1: Summary of Re numbers, inlet velocity (V_{in}), vortex shedding period (VSP), Strouhal number (St), and the vortex shedding interval (VSI) that snapshots were chosen within for the flow past a single cylinder cases considered

Re	V_{in} (m/s)	VSP (s)	St	VSI (s)
2900	0.0424	49.65	0.23	[790, 839.65]
3500	0.0511	43.15	0.22	[989.35, 1032.5]
4800	0.0701	33.4	0.21	[716.7, 750.1]
5500	0.0803	29.9	0.20	[586.6, 616.5]
6000	0.0876	28	0.20	[774, 802]
6600	0.0964	26.5	0.19	[476.5, 503]
7190	0.105	23.8	0.20	[774.5, 798.3]

with a Re number of 4800 shown in Figure 2.2. As an example, the final column of Table 2.1 shows the time interval of the vortex shedding period used for the case of flow past a single cylinder corresponding to each Re number.

For all Galerkin projection ROM analyses, a standard Runge-Kutta nonlinear initial value differential equation solver was used to solve the ODEs described in Equation **??**. To evaluate the accuracy of the results of all ROM analyses (Galerkin projection and surrogate modeling), the predicted velocity fields were compared to the corresponding URANS full-order model (FOM) velocity fields through the following error metric:

$$Error(\vec{\gamma}) = \frac{||u^{FOM}(\vec{x},\vec{\gamma}) - u^{ROM}(\vec{x},\vec{\gamma})||}{||u^{FOM}(\vec{x},\vec{\gamma})||}, \tag{2.21}$$

where $u^{FOM}(\vec{x},\vec{\gamma})$ and $u^{ROM}(\vec{x},\vec{\gamma})$ are the velocity fields estimated by the FOM and ROM, respectively (note again that $\vec{\gamma}$ is the set of input parameters, including the specified time point and Re number), and $||\cdot||$ represents a specified metric norm, with both the L_2 and L_∞ norms being used for the results presented in the following.

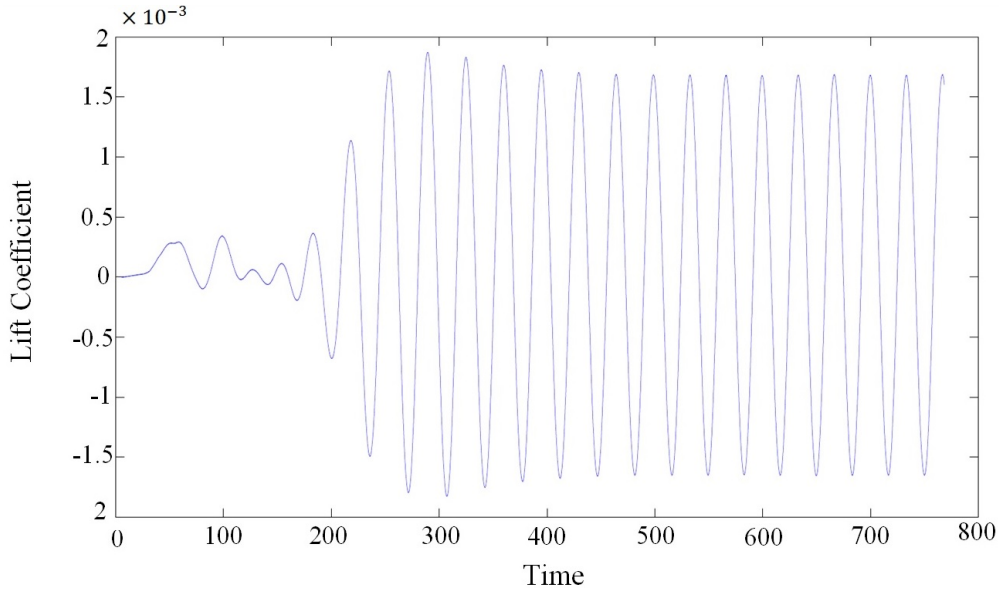

Figure 2.2: The variation of the lift coefficient on the cylinder for flow past a single cylinder at Re=4800.

Results of flow past a single cylinder are presented in Section 2.4.1. First, in Section 2.4.1 the various ROM strategies were analyzed for applicability to flow past a single cylinder considering prediction of velocity fields at different time levels for fixed Re numbers. Then, in Section 2.4.1.2, using a GPOD technique, ROMs were created to be valid for a range of Re numbers, and their corresponding accuracy was tested. At the end of the Section 2.4.1.2 the dependence of the size of the snapshot set on the resulting ROM accuracy was also evaluated. Section 2.4.2 presents the results for flow past a cluster of four cylinders. Similarly, prediction in time was considered for the multiple cylinder case first in Section 2.4.2.1, which was followed by prediction across time and Re number in Section 2.4.2.2.

2.4.1 Example 1: Flow Past a Single Cylinder

This example consisted of a single rigid cylinder of radius $0.5m$ located at the center of a cylindrical fluid domain, with a uniform inlet velocity boundary condition specifies a constant horizontal fluid flow velocity applied to the left half of the cylinder as specified in Table 2.1,

and a pressure boundary condition of fixed static pressure of the environment into which flow exhausts is applied to the right half of the cylinder. The size of the fluid domain was chosen so that no fluctuation of flow fields can be seen close to the boundaries. Figure 2.3 shows a schematic for the first test case.

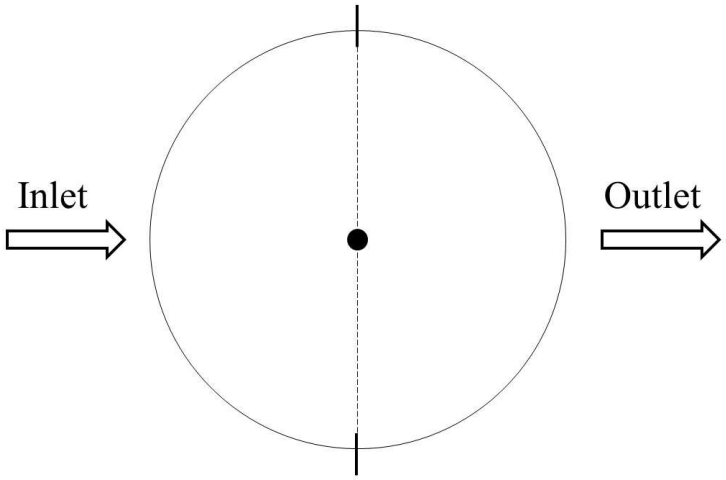

Figure 2.3: Schematic for flow past a single cylinder. The small filled circle represents the cross section of the cylinder with radius of 0.5m and the larger circle shows the fluid domain of interest with radius of 50m.

2.4.1.1 Predicting time variation for fixed Re numbers: For the first set of tests, POD was applied separately to each set of 15 snapshots corresponding to a separate Re number (i.e., POD was applied seven separate times to obtain modes). Figure 2.4 shows a representative example of the first four modes (i.e., modes with four highest corresponding eigenvalue from highest to lowest) obtained for the analysis with Re number 2900 and Figure 2.5 shows examples of the cumulative modal energy for Re numbers 5500, 4800, and 3300. The cumulative modal energy for the K^{th} mode from the set of n modes can be calculated as follows (note the modes are numbered from highest eigenvalue magnitude to lowest):

$$CM(K) = \frac{\sum_{j=1}^{K} \lambda^{(j)}}{\sum_{i=1}^{n} \lambda^{(i)}}. \tag{2.22}$$

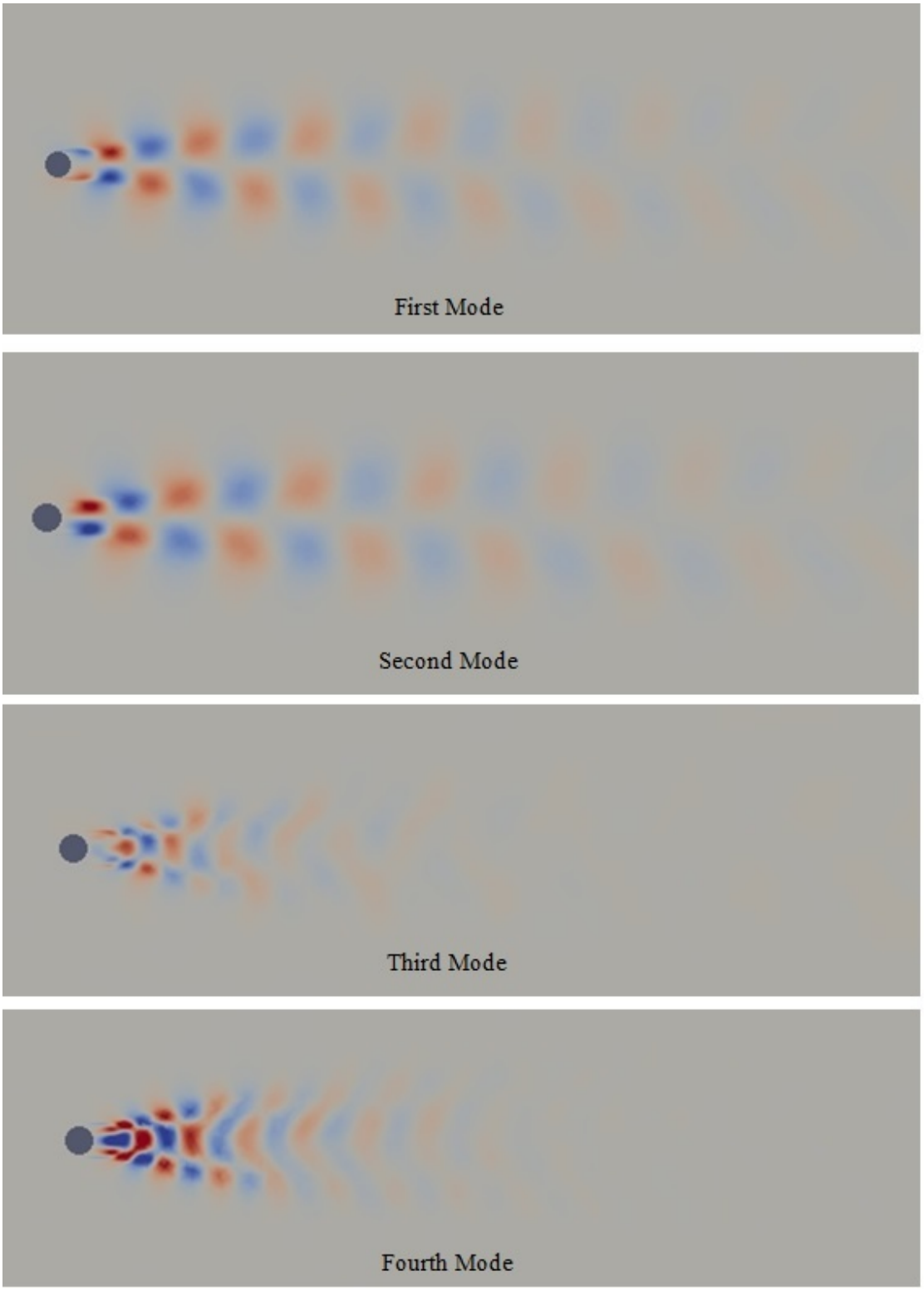

Figure 2.4: The first four POD modes for flow past a single cylinder at Re =2900 (Note that the color contours represent the amplitude of the POD mode).

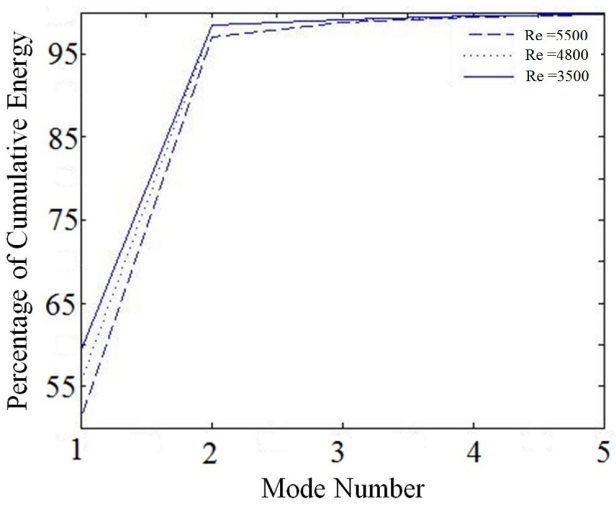

Figure 2.5: The convergence of percentage of cumulative energy corresponding to each eigenvalue for three simulations of flow past a cylinder.

One point of interest is that the first two and second two modes appear to form pairs in a sense, with one seeming to be close to the mirror image of the other, which was similar for the other Re numbers considered. In addition, the first two modes of all cases captured the majority of the energy of the systems (over 95%), and four modes were sufficient in all cases to capture more than 99% of the cumulative modal energy. However, this may change for Re numbers greater than those considered, as it can be seen that the rate of convergence of the cumulative modal energy decreases as the Re number increases, with the higher numbered modes becoming more important to capturing the system behavior at higher Re numbers.

Using the four highest energy POD modes obtained, both the Galerkin projection method and the surrogate model method were applied to create ROMs to predict the time variation of the flow velocity for each Re number separately. For the surrogate modeling method, the modal coefficients were interpolated/extrapolated using a Gaussian RBF and the Kriging approach described with $d = 4$. Each approach was applied to predict the response at four time levels that were not included in the original snapshot sets: three that were within the bounds of the corresponding vortex shedding interval (i.e., interpolation) and one outside of that interval (i.e., extrapolation). The L_2 and L_∞ errors of each prediction were calculated

and their corresponding averages over the four test times are summarized in Table 2.2 for three representative Re numbers for each approach.

Both surrogate model approaches produced nearly the same error levels for all Re numbers considered, and had significantly lower error than the Galerkin projection for all cases. However, the error for the surrogate model methods increased significantly as the Re number increased, with the error levels at the highest Re number being on the same level as the Galerkin projection results. In contrast, the error in the Galerkin projection appeared to be highly consistent and independent of Re number. The increased error in the Galerkin projection compared to the surrogate model methods is not necessarily unexpected since the snapshots and test sets were generated with URANS simulation while the Galerkin projection is applied to the standard NS equations (which are not solved exactly with a URANS result). The relative simplicity of this single cylinder example also likely contributes to the capability of the surrogate model methods to produce accurate results, which would explain the decrease in accuracy as the flow becomes more complex with increasing Re number. Furthermore, if the observed pattern continued, it would be expected that the Galerkin projection results would begin to become comparatively more accurate than those from a surrogate model for larger Re numbers. Yet, overall for the cases considered, all ROM approaches produced relatively accurate and consistent (all variances in the errors were also low) estimates of the time variation of flow fields around a single cylinder at various fixed Re numbers. Moreover, these relatively accurate ROM results were achieved at a substantially lower computational cost than the URANS FOM. For example, the Galerkin projection ROM for a single Re number (which is orders of magnitude more computationally expensive than the surrogate model approaches) required less than 10 seconds of computing time on a standard PC compared to more than 24 hours for URANS on the same machine.

2.4.1.2 Predicting variations in time and Re number: To evaluate the capability of the ROM approaches to predict flow fields at varying Re number in addition to time, for the second set of tests the time samples at multiple Re numbers were combined into one snapshot set for POD, and these modes were applied to predict the response in time for new Re numbers (not included in the snapshot set). Note that this does not affect the

Table 2.2: The average L_2 and L_∞ errors for the ROM response predictions by the POD Galerkin (Galerkin) and surrogate model (surrogate) methods over the four given test times for three representative Re numbers for flow past a single cylinder

Re	Test Times	L_2 (%)		L_∞ (%)	
		Galerkin	Surrogate	Galerkin	Surrogate
2900	795.95 808.37 834.71 842.13	4.02	Gaussian RBF: 0.03 Kriging: 0.03	5.44	Gaussian RBF: 0.05 Kriging: 0.05
5500	593.62 600.64 604.65 619.55	5.55	Gaussian RBF: 0.78 Kriging: 0.77	5.93	Gaussian RBF: 0.86 Kriging: 0.91
7190	780.92 787.35 796.15 800.20	4.26	Gaussian RBF: 3.93 Kriging: 4.12	4.78	Gaussian RBF: 4.18 Kriging: 4.29

implementation of the Galerkin projection approach, but for the surrogate model approaches Re number is now part of the input of the interpolation/extrapolation equations in addition to time to estimate the modal coefficient variations. Four different test cases were considered, each with a different set of Re numbers from the original dataset (Table 2.1) used to create the combined snapshot set and with the remaining Re numbers used as the test set to calculate the prediction errors. The first three test cases all considered interpolation of Re number (i.e., the Re numbers in the snapshots bounded those in the test sets), while the final test considered extrapolation.

The first test case included five Re numbers in the snapshot set: 2900, 3500, 5500, 6000, and 7190, for a total of 75 snapshots (in time and Re number). In contrast to the previous examples that considered each Re number separately, considerably more modes were required to capture the majority of the system energy, with 12 modes being needed in this case to capture more than 99% of the system energy. For an example of the modal characteristics, Figure 2.7 shows the first 6 highest energy modes for this case. These modes obtained for multiple Re numbers were similar to those shown for a single Re number, but with more

mirrored pairs in the set from multiple Re numbers. Using the first 12 modes, the Galerkin projection and surrogate model methods were then applied to predict the response at four time levels for the two Re numbers not included in the snapshot set: 4800 and 6600. Again, a Gaussian RBF and the Kriging approach were considered for the surrogate modeling, with $d = 4$ for the Kriging method. Table 2.3 summarizes the average (over time) L_2 and L_∞ errors for the Galerkin projection prediction at the two new Re numbers. However, the results for the surrogate modeling are not shown since the prediction errors were all in excess of 100%, and thus not informative in detail. The surrogate modeling becoming ineffective highlights the limitations of these approaches. For perspective, Figure 2.6 shows the variation of the first modal coefficient with respect to time and Re number estimated by the surrogate model with Kriging compared to the Galerkin projection results (noting that the Galerkin projection is substantially more accurate). Even with an increase in dimensionality of the input of only one, the relatively small increase in the dataset (i.e., number of snapshots) is insufficient to facilitate the regression to capture the increased complexity of the response surface with the surrogate model. In stark contrast, the accuracy of the Galerkin projection approach for predicting Re number variations is nearly equivalent to that for fixed Re numbers. The Galerkin projection results were also highly consistent again, with low error variances over time.

The second and third test cases considered the effect of the number/diversity of snapshots on the prediction capability of the Galerkin projection approach. The second test case included four Re numbers in the snapshot set: 2900, 4800, 6000, and 7190, for a total of 60 snapshots. The third test case included three Re numbers: 2900, 5500, and 7190, for a total of 45 snapshots. For consistency, the first 12 modes were again utilized for the ROM in both test cases (with 12 clearly exceeding 99% of the system energy in both cases). Tables 2.4 and 2.5 summarize the average L_2 and L_∞ errors for the Galerkin projection prediction at the new Re numbers for the second and third test cases, respectively. The accuracy of the test case with four Re numbers in the snapshot set is again consistent with the previous Galerkin projection results presented, and the errors can be considered relatively low. However, the error increased significantly when the number of Re numbers included in the snapshot set dropped to three, with the error for the two higher Re numbers even exceeding 10%.

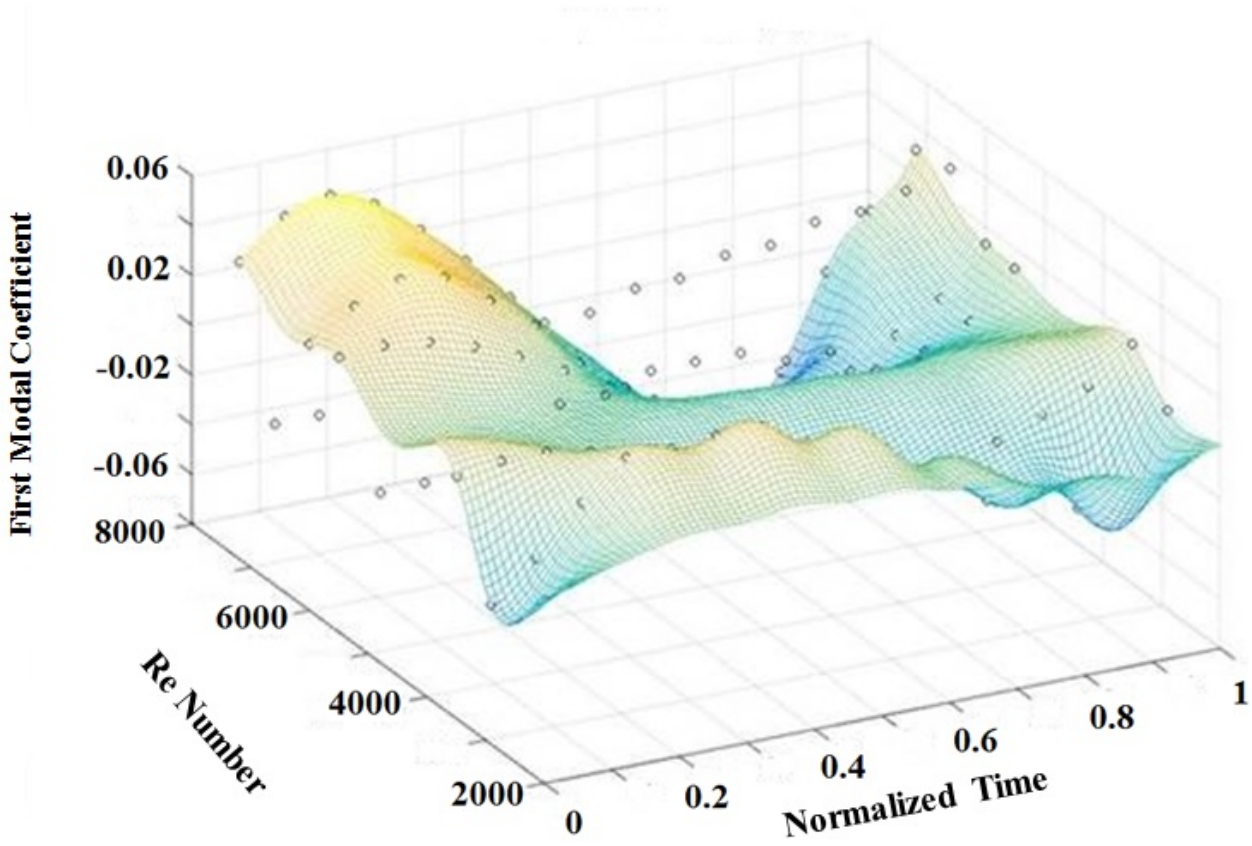

Figure 2.6: The variation of the first modal coefficient with respect to time and Re number predicted by the POD-Galerkin ROM (colored mesh) and Kriging surrogate model ROM (black circles).

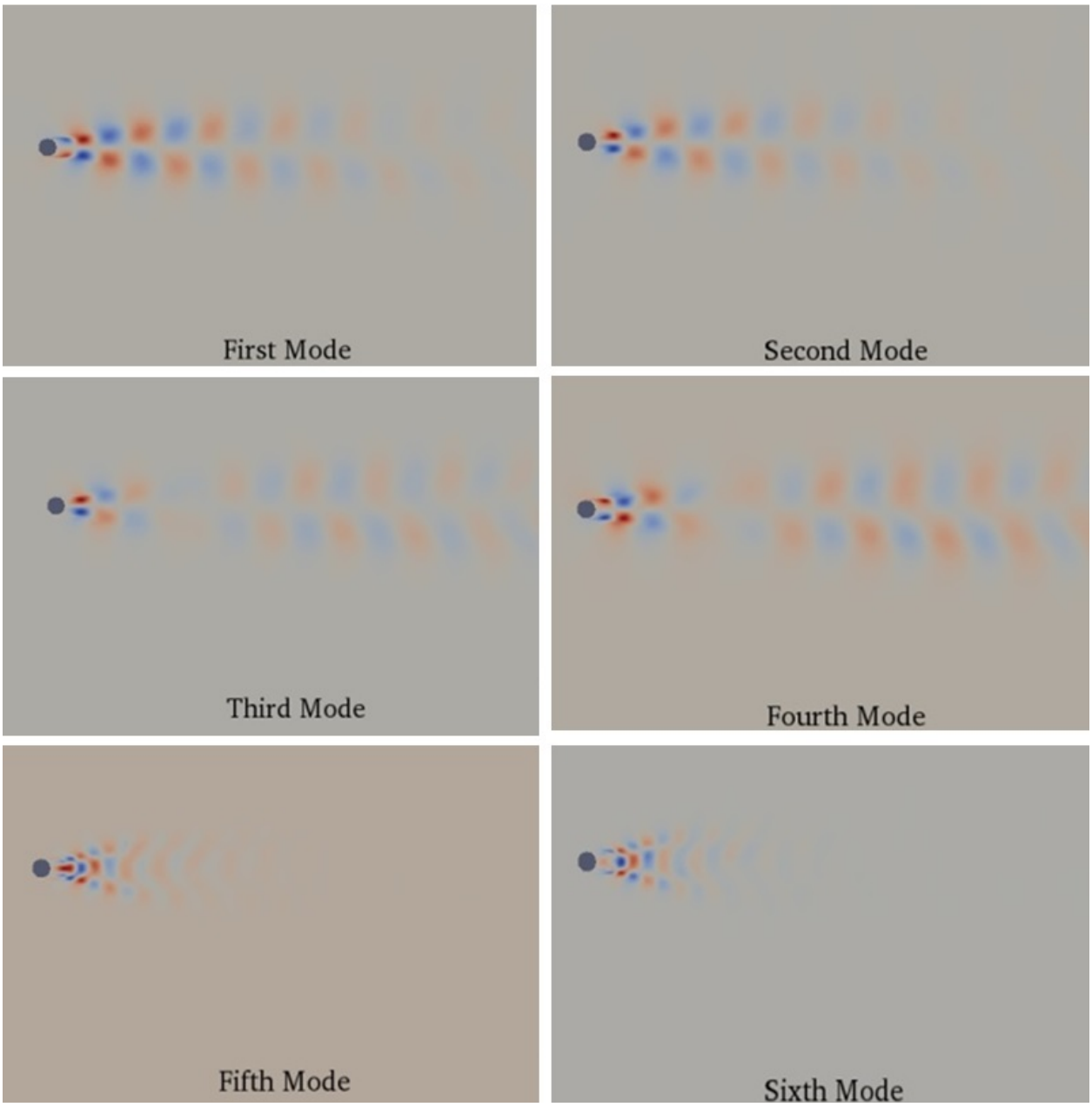

Figure 2.7: The first six POD modes for flow past a single cylinder obtained from the ensemble of 75 snapshots from Re numbers 2900, 3500, 5500, 6000, and 7190 (Note that the color contours represent the amplitude of the POD mode).

Table 2.3: The average L_2 and L_∞ errors for the POD Galerkin ROM obtained from the ensemble of snapshots from Re numbers 2900, 3500, 5500, 6000, and 7190, for the given Re numbers over the four given test times for flow past a single cylinder.

Re	Test Times				L_2 (%)	L_∞ (%)
4800	481.8	487.1	492.4	497.7	5.61	6.01
6600	723.3	730.6	736.7	743.4	5.77	6.79

Although this third test case included only one less Re number in the snapshot set, the error more than doubled for some predictions.

The fourth and final test case examined the capability of the Galerkin projection ROM to extrapolate in Re number. As such, four Re numbers were included in the snapshot set: 2900, 3500, 4800, and 5500, and two larger Re numbers were used to test the ROM accuracy: 6000 and 6600. Table 2.6 again summarizes the average errors in the ROM predictions with the first 12 modes for the four test times with the two test Re numbers. While four Re numbers in the snapshot set had relatively low error previously for the Re interpolation test (Table 2.4), with the same snapshot set size the error increased significantly for estimating Re numbers outside of the range of those included in the snapshot set. Although, the level of error in this example may be acceptable for many applications, it is important to note that the ability to extrapolate in Re number is limited, and the error appears to increase as the Re number becomes farther from the range included in the snapshot set.

2.4.2 Example 2: Flow Past a Cluster of Four Cylinders

To take a step toward understanding the capability of POD-based ROMs for approximating turbulent flows in more complex systems than flow past a single cylinder (such as the reactor lower plenum example shown in Figure 2.1), an example of flow past a cluster of four cylinders was considered. Figure 2.8 shows a schematic of this multiple-cylinder example. The four cylinders were arranged in a $2m \times 2m$ square pattern with two cylinders centered on each

Table 2.4: The average L_2 and L_∞ errors for the POD Galerkin ROM obtained from the ensemble of snapshots from Re numbers 2900, 4800, 6000, and 7190, for the given Re numbers over the four given test times for flow past a single cylinder

Re	Test Times				L_2 (%)	L_∞ (%)
3500	997.98	1006.61	1015.24	1023.87	4.27	4.97
5500	592.58	598.56	604.54	610.52	6.58	7.36
6600	481.82	487.14	492.47	497.70	5.89	6.12

Table 2.5: The average L_2 and L_∞ errors for the POD Galerkin ROM obtained from the ensemble of snapshots from Re numbers 2900, 5500, and 7190, for the given Re numbers over the four given test times for flow past a single cylinder.

Re	Test Times				L_2 (%)	L_∞ (%)
3500	997.98	1006.61	1015.24	1023.87	8.65	8.89
4800	723.38	730.06	736.74	743.42	7.97	8.91
6000	779.63	785.21	790.85	796.44	10.24	12.36
6600	481.82	487.14	492.47	497.70	12.01	12.49

Table 2.6: The average L_2 and L_∞ errors for the POD Galerkin ROM obtained from the ensemble of snapshots from Re numbers 2900, 3500, 4800, and 5500, for the given Re numbers over the four given test times for flow past a single cylinder

Re	Test Times				L2 (%)	Linf (%)
6000	779.63	785.21	790.85	796.44	8.24	9.37
6600	481.82	487.14	492.47	497.70	10.09	14.29

axis, and the same sized fluid domain and inlet/outlet conditions were applied as were used for the single-cylinder tests. The time variation of the lift coefficient of the nearest cylinder to the inlet was utilized to define the vortex shedding period for the snapshot sampling process.

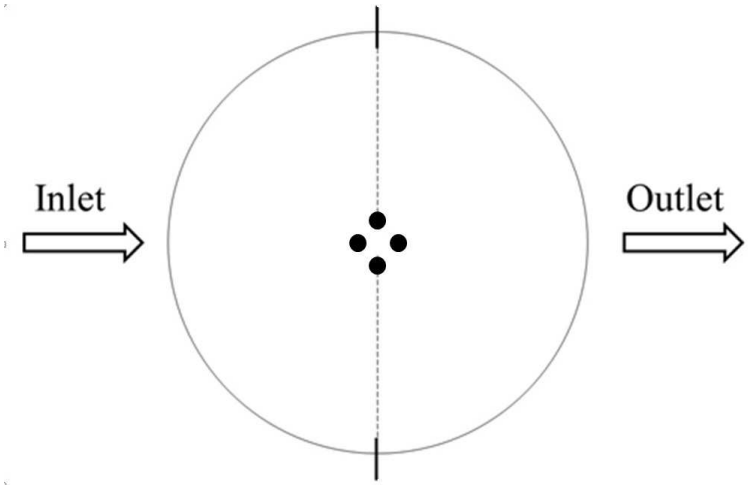

Figure 2.8: Schematic for flow past a cluster of four cylinders. The small filled circles represents the cross section of the cylinders with radius of 0.5m each which were located on the vertices of a 2m $\times$ 2m square,and the larger circle shows the fluid domain of interest with radius of 50m.

2.4.2.1 Predicting time variations for fixed Re numbers: Figure 2.9 shows a representative example of the first two highest energy POD modes obtained for the analysis with Re number 5500. As would be expected, the spatial distributions of the modes are considerably more complex than those for the single cylinder examples. However, the first two modes were similarly dominant, capturing over 84% of the total system energy for this example.

As before, using the eight highest energy POD modes obtained, both the Galerkin projection method and the surrogate model method were applied to create ROMs to predict the time variation of the flow velocity around the four cylinders for each Re number separately. Again, a Gaussian RBF and the Kriging approach with $d = 4$ were used for the surrogate

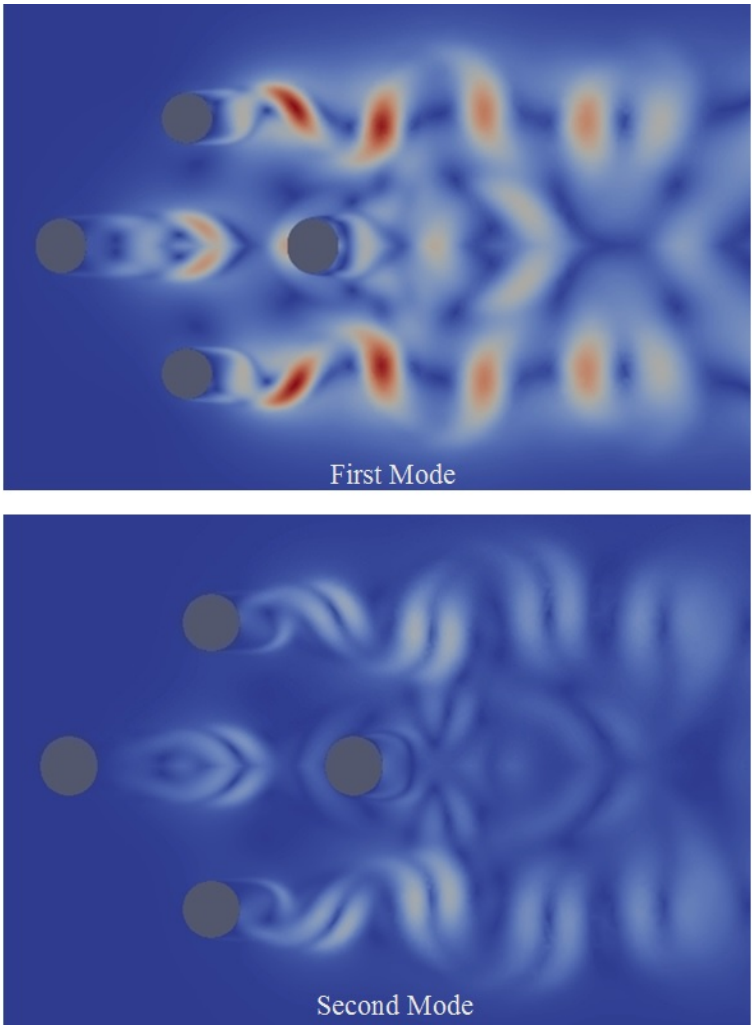

Figure 2.9: The first two POD modes for flow past multiple cylinders at Re =5500 (Note that the color contours represent the amplitude of the POD mode).

Table 2.7: The average L_2 and L_∞ errors for the ROM response predictions by the POD Galerkin (Galerkin) and surrogate model (surrogate) methods over the four test times for three representative Re numbers for flow past a cluster of four cylinders.

Re	L2 (%)			Linf (%)		
	Galerkin	Surrogate		Galerkin	Surrogate	
2900	5.19	Gaussian RBF:	6.24	5.75	Gaussian RBF:	7.49
		Kriging:	4.97		Kriging:	6.12
5500	5.74	Gaussian RBF:	5.16	6.22	Gaussian RBF:	6.38
		Kriging:	5.05		Kriging:	5.76
7190	5.86	Gaussian RBF:	5.60	6.18	Gaussian RBF:	6.21
		Kriging:	4.44		Kriging:	6.03

modeling. The L_2 and L_∞ errors of each prediction were calculated and their corresponding averages over the four test times (three interpolation and one extrapolation) are summarized in Table 2.7 for three representative Re numbers for each approach. Of note is that the error of the Galerkin projection method is only a relatively small amount larger than for the equivalent results for the single-cylinder example (i.e., the accuracy is almost the same). Alternatively, the increased complexity of this example case led to a significantly more substantial increase in the error of the surrogate modeling results compared to the single cylinder example. In particular, the accuracy of the Gaussian RBF surrogate model was actually less than the Galerkin projection method in some cases. The Kriging approach was consistently more accurate than both other methods, but only by a relatively small amount.

2.4.2.2 Predicting variations in time and Re number: For the final test case, the capability of the POD-Galerkin ROM approach to predict flow variations with respect to changes in both time and Re number for flow past the cluster of four cylinders was evaluated. Note that the surrogate model approaches were again inadequate for the case of varying Re

number, and are thus not discussed further. This test case included five Re numbers in the snapshot set: 2900, 3500, 4800, 6000, and 6600, for a total of 75 snapshots. Then, the accuracy of the POD-Galerkin ROM with the 15 highest energy modes was evaluated for again predicting the response at four time levels for two Re numbers not included in the snapshot set: 5500 (i.e., interpolation of Re number) and 7190 (i.e., extrapolation of Re number).

Table 2.8 summarizes the average L_2 and L_∞ errors for the Galerkin projection prediction at the two new Re numbers for flow past the four cylinders. The accuracy of the POD-Galerkin ROM was again highly consistent with the previous single-cylinder test cases, regardless of the increase in complexity of the problem. Highlighting the potential of this ROM approach, the error for Re number interpolation was lower than the equivalent prediction for the single cylinder example. However, extrapolation in Re number again showed a marked decrease in the accuracy of the ROM prediction compared to interpolation.

Table 2.8: The average L_2 and L_∞ errors for the POD Galerkin ROM obtained from the ensemble of snapshots from Re numbers 2900, 3500, 4800, 6000 and 6600, for the given Re numbers over the four test times for flow past a cluster of four cylinders.

Re	L2 (%)	Linf (%)
5500	5.20	6.07
7190	9.48	10.12

2.5 CONCLUSIONS

Two different approaches for proper orthogonal decomposition-based model reduction for simulating turbulent flows were presented and numerically evaluated: (1) a Galerkin projection of the Navier-Stokes equations onto a POD basis, which sacrifices some computational efficiency to incorporate the physics of the system into the ROM, and (2) a surrogate modeling approach, which achieves a relatively higher computational efficiency, but replaces the

governing equations of fluid dynamics with a regression based mapping between the input parameters and POD modal reconstruction coefficients. For the numerical evaluation, two different test cases were considered to examine the potential accuracy of the ROM approaches for turbulent flows: (1) flow past a single cylinder, which is a simple and well-studied test case, and (2) a significantly more complex system of flow past a cluster of four cylinders. Furthermore, these numerical tests focused on the capabilities of the ROMs for a range of Reynolds numbers in the turbulent regime, as well as predictions of flow fields with respect to time. In all test cases when predicting the time variation of the flow fields around a single cylinder for a fixed Re number, the surrogate model approach produced significantly lower error than the Galerkin projection approach, although all ROMs were relatively accurate (and a substantial savings in computational cost compared to FOMs). However, when the system complexity increased for the four-cylinder case, the error for the surrogate model predictions in time for fixed Re number increased significantly, while the error of the Galerkin projection was more similar to that of the single cylinder results, and was lower than the surrogate model method in some cases. Moreover, in all cases (both single-cylinder and four-cylinder) when the ROM input was expanded to include both time and Re number, the results of the surrogate model approach were unacceptable (i.e., errors greater than 100%), while the Galerkin projection approach was able to again produce consistently accurate predictions. Additional tests showed that the ROM error increased significantly (by nearly a factor of 2) when extrapolating in Re number compared to interpolating, and this error was further sensitive to the number of Re numbers used to produce the initial snapshot sets. An important final note is that the accuracy of the Galerkin projection could likely be increased even further by utilizing snapshots generated from direct numerical simulation of the NS equations, rather than URANS that was utilized in the present study.

3.0 REDUCED-ORDER MODELING FOR COMPUTATIONAL SOLUTION OF CONTROL PROBLEMS FOR ROTARY CYLINDERS IN FLUID FLOWS

3.1 ABSTRACT

An approach for utilizing reduced-order modeling within a computational procedure to optimally control rotary cylinders for drag reduction in fluid flows is presented and numerically evaluated. More specifically, the objective of the optimal control problem considered is reduction of the drag coefficient acting on one or more embedded cylinders while simultaneously utilizing the least amount of energy through control of the rotational velocity of the cylinder(s) for a specified flow through a channel. The effect of the pressure field on the drag on the cylinder(s) is included in the objective, in addition to the effect of the fluid velocity gradient, to provide a physically accurate measure of the drag. For the reduced-order modeling, the proper orthogonal decomposition (POD) method is utilized to obtain a low dimensional basis (i.e., modes) from a previously obtained set of representative velocity fields for the system (e.g., velocity fields previously obtained from standard computational fluid dynamics solutions with potential control parameter realizations). Then, a reduced-order model for simulating the flow past cylinders for any potential set of control parameters is created through a Galerkin projection of the Navier-Stokes equations onto the POD basis. Lastly, the optimal control problem is formulated in terms of the POD modal coefficients and gradient-based optimization with the adjoint method is used to estimate an optimal control solution. Two simulated case studies are presented to evaluate the computational procedure: the first involving flow past a single rotary cylinder and the second involving flow past two in-line rotary cylinders. In all test cases the solution procedure is shown to determine a set of control parameters to substantially reduce the drag coefficient of the system with

significantly less computational expense than if standard computational fluid dynamics had been used. In addition, a significant tradeoff is shown between the objective of reducing the drag coefficient and the objective of minimizing the energy cost of rotating the cylinder(s), particularly for the two-cylinder case.

3.2 INTRODUCTION

The ability to control flow fields is important in many engineering applications, such as microfluidic devices [36] and transportation systems [58]. The main objective of flow control is to act on a fluid system at a few selected locations, and/or by altering boundary conditions of the system (e.g., inlet velocity, outlet pressure, moving wall boundaries, etc.) to obtain/maintain a desired behavior while keeping the cost of the alteration as low as possible. In flow control problems the state equations used are typically Navier-Stokes equations and the time interval involved is often very large. Therefore, standard numerical methods, such as the finite element method or finite difference method are computationally prohibitive in these types of problems. Furthermore, although there are some strategies for the problem of flow control that are based on linearized Navier-Stokes equations, which are applicable for a large class of control techniques [52], many of these strategies are limited to relatively low-dimensional systems (i.e., $\mathcal{O}(10^3)$), while the numerical discretization of fluid flows invariably result in much larger dimensional systems, typically $\mathcal{O}(10^6)$. Thus, model reduction has an undeniable role in solving flow control problems.

There are several approaches to create accurate reduced-order models (ROMs) of physical systems with significantly reduced computational expense compared to standard full-order modeling (e.g., finite element method). One promising ROM approach (as will be focused on in the present work) does not replace the physics-derived governing equations of the system, as is the case for surrogate- (i.e. meta-) modeling methods, and instead is based on projecting the governing equations (e.g., Navier-Stokes equations) onto subspaces consisting of basis elements (i.e., reduced basis functions) that are derived to contain characteristics of the expected solution. This is in contrast to finite element (or similar) techniques, where the

elements of the subspaces are not necessary related to the physical properties of the system that they approximate. There are numerous methods for obtaining such reduced-basis functions, such as: Lagrange basis [96], Hermite basis [49], Taylor basis [85], Proper Orthogonal Decomposition (POD) [75], Krylov subspace [111], Centroidal Voronoi Tessellations (CVT) [19], etc. POD bases are used in this paper due to their optimality in the sense of minimizing the average L_2 error and its convergence properties [48]. Furthermore, in the present work the POD bases are obtained from solutions of a full-order model (i.e., using a finite element solver, finite volume solver, etc), referred to as snapshots. The POD method can be viewed as a technique to remove redundant information or compress the information that the snapshots contain to produce a basis. Naturally, the ability of the POD modes to represent the system is limited by the original snapshots that are used. Therefore, generating informative snapshots that are representative of the overall system is crucial in creating generalized ROMs that can be applied later to solve control problems.

The POD-Galerkin projection approach for creating ROMs of fluid flows was first developed by Lumely [74], and it has been popular in recent years for dealing with control problems of fluid flows. There are several studies that utilized the POD-Galerkin projection approach for flow control problems, such as optimal control of flow over a backward-facing step [88], control of flow around a circular cylinder by a synthetic jet positioned at the back stagnation point [34], and control of the Burger's equation [55]. Bergmann and Brancher [13] used an ad-hoc time-dependent excitation that is rich in transients to generate snapshots to then obtain POD modes to create the ROM. Bergmann and Cordier [14] proposed a Trust-Region Proper Orthogonal Decomposition (TRPOD) approach, which was originally introduced by Fahl [33], to update ROMs during the optimization process. The present investigation utilizes the global POD method (GPOD) [106] to generate informative snapshots that will produce ROMs suitable for control optimization. The basic idea behind the GPOD approach is to enrich the snapshot matrix with solutions corresponding to different values of the variable system parameters, so that the POD bases obtained from these snapshots can represent the system for a broad range of these parameters. The benefit of using GPOD in constructing ROMs over some of the alternatives mentioned is that there is no need to update the ROM at each step of the optimization process. Once the ROM is built based

on GPOD, it can be used for (almost) any new system parameter without any updating or interpolation.

The present work is particularly focused on flow control problems with the objective of reducing the drag force on a bluff body. When the flow separates from a bluff body, the resulting wake exhibits vortex shedding, which leads to a sharp rise in drag, noise, and fluid-induced vibration [38]. The key motivation in research on drag reduction is to develop new technology that will result in the design of flow systems with significantly lower fuel consumption. In particular, the present work focuses on control of flow around circular cylinder(s) by rotating the cylinder(s). This example was chosen as the single-cylinder case is a relatively well-studied benchmark problem, while the multiple-cylinder case allows for a novel exploration of the potential for more complex systems. As noted, the present study utilized the GPOD technique and Galerkin projection to create ROMs for simulating these fluid systems. In addition, a snapshot modification strategy was used to produce modes with homogeneous boundary conditions and avoid inclusion of the pressure field in the ROM, which further improves computational efficiency [82]. Moreover, in contrast to much of the related flow control work, in the present study the pressure field on the cylinder(s) was calculated through a post-processing step to include in the control objective functional. By including the pressure term in addition to the velocity gradient, a more accurate estimate of the drag coefficient (and its potential reduction through control) can be calculated. Section 3.3 describes the forward problem used for simulating flow around one or more cylinders and the control objective functional based on these flow fields to be optimized. Then, Section 3.4 presents the ROM approach for flow around a stationary cylinder, followed by the necessary modifications to account for rotary cylinders. Section 3.5 presents the optimization-based formulation and solution strategy for the optimal control problem with the ROM. Lastly, Section 3.6 presents and discusses a series of numerical examples displaying the capabilities of the ROM optimal control strategy, which is followed by the concluding remarks in Section 3.7.

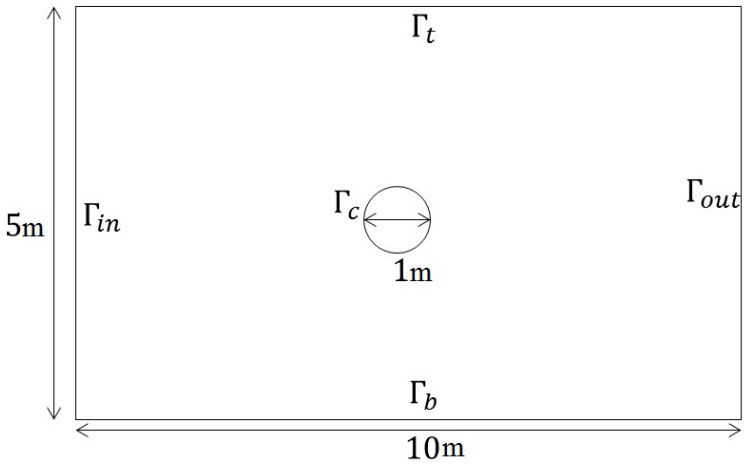

Figure 3.1: Schematic for flow past a cylinder in a channel.

3.3 FORWARD PROBLEM AND CONTROL OBJECTIVE

Figure 3.1 shows a schematic of the two dimensional flow past a cylinder problem considered herein for the case of a single rotating cylinder (noting it can generalized in the same format to multiple cylinders). Assuming incompressibility, the forward problem used herein to describe flow past a rotating cylinder can be described by the unsteady Navier-Stokes equations as:

$$\rho(\frac{\partial}{\partial t}\vec{u}(\vec{x},t) + \vec{u}(\vec{x},t)\cdot\nabla\vec{u}(\vec{x},t)) = -\nabla p(\vec{x},t) + \mu\nabla^2\vec{u}(\vec{x},t) \tag{3.1}$$

$$\rho\nabla\cdot\vec{u}(\vec{x},t) = 0, \tag{3.2}$$

where $\vec{u}(\vec{x},t)$ is the fluid velocity vector, p is the pressure field, ρ is the fluid's density, and, μ is fluid viscosity. The boundary conditions considered, including rotation of the cylinder, can be shown as follows:

$$\vec{u}(\vec{x},t) = C\boldsymbol{e}_1, \quad \forall\vec{x}\in\Gamma_{in} \tag{3.3}$$

$$\vec{u}(\vec{x},t) = 0, \quad \forall\vec{x}\in\Gamma_t \text{ and } \vec{x}\in\Gamma_b \tag{3.4}$$

$$\frac{\partial u_2(\vec{x},t)}{\partial x_1} = 0 \text{ and } p - \frac{1}{Re}\frac{\partial u_1(\vec{x},t)}{\partial x_1} = 0, \quad \forall \vec{x} \in \Gamma_{out} \tag{3.5}$$

$$\vec{u}(\vec{x},t) = \Theta_r \boldsymbol{e_\theta}, \quad \forall \vec{x} \in \Gamma_c, \tag{3.6}$$

where C is the magnitude of the inlet velocity of the flow and Θ_r is the rotational velocity, which can be formulated as follows:

$$\Theta_r(t) = Asin(\omega t), \tag{3.7}$$

where A is the amplitude and ω is the frequency of the cylinder rotational velocity.

Based on the forward problem defined, the optimal control problem considered herein was defined as an optimization problem to find values for A and ω to minimize the drag on the cylinder. In addition, since the purpose of drag minimization is often intended to decrease energy consumption of the system, the energy used to rotate the system should also be minimized. Therefore the objective functional of the optimal control problem was defined as:

$$J(A,\omega) = \int_0^T C_D(t)dt + \alpha \int_0^T \frac{\Theta_r(t)}{C}dt, \tag{3.8}$$

where C_D is the drag coefficient which is a function of the fluid material properties, pressure, and velocity around the cylinder (note: a specific C_D definition is provided in the example section). The second term in Equation 3.8 quantifies the energy required to rotate the cylinder, and the contribution of this objective to the optimization is controlled through the penalization factor α, so that the trade-off between the drag reduction and the energy used to rotate the cylinder can be investigated.

The optimal control problem can be solved using any preferred optimization strategy such as stochastic search methods or gradient-based methods [79]. However, due to the relatively high computational expense of the forward problem, some form of model reduction is necessary for this solution strategy to be practical in many applications. The following section describes the POD-Galerkin projection approach for model reduction of flow past a

cylinder in a channel (i.e., the forward problem). The methodology is first presented for a stationary cylinder case, and then extended for the case of rotating cylinder.

3.4 POD-GALERKIN PROJECTION APPROACH FOR ROM

The core hypothesis of the POD-Galerkin projection approach for reduced-order modeling is that a relatively small number of full-order (i.e., traditional CFD solvers) analyses based upon different values of the control parameters of interest contain fundamental information about the potential solution fields of the boundary value problem (BVP) and can be used to derive a low-dimensional basis that can predict the BVP solution fields for a range of control parameters (not just the specific parameter values used to generate the set of full-order analyses) with reasonably sufficient accuracy. As such, the POD-Galerkin projection approach to create a ROM is a two-step process: (1) apply POD to the previously obtained full-order model response field to obtain a basis and (2) apply Galerkin-projection of the BVP governing equation onto the POD basis.

3.4.1 POD Basis Generation

The POD approach specifically derives the low-dimensional basis such that the difference between the original full-order data and the best approximation to that data with this basis is minimized in an L_2 average sense. This problem of determining the POD basis can be cast as an optimization problem to determine the set of m modes $\{\vec{\phi}_i(\vec{x})\}_{i=1}^{m}$ given a set of n full-order analysis fields $\{\vec{u}(\vec{x},\vec{\gamma}_k)\}_{k=1}^{n}$, where $\vec{\gamma}_k$ is the k^{th} vector of the input parameters of interest, such that the average L_2-error between full-order analyses and their projection on to the subspace is minimized. Through several manipulations, including applying the method of snapshots [103], the POD optimization problem can be transformed into the following n-dimensional eigenvalue problem:

$$\frac{1}{n}\sum_{k=1}^{n} A_{jk}C_k = \lambda C_j, \tag{3.9}$$

where

$$A_{jk} = \int_{\Omega} \vec{u}(\vec{x}, \vec{\gamma}_j) \cdot \vec{u}(\vec{x}, \vec{\gamma}_k) d\vec{x}. \tag{3.10}$$

An optimal set of as many as n orthogonal basis functions (i.e., POD modes) can then be determined from the solution of the above eigenvalue problem by:

$$\vec{\phi}_i(\vec{x}) = \frac{1}{\lambda^{(i)} n} \sum_{k=1}^{n} \vec{u}(\vec{x}, \vec{\gamma}_k) C_k^{(i)}, \quad \text{for } i = 1, 2, ..., n, \tag{3.11}$$

where $C_k^{(i)}$ is the k^{th} component of the i^{th} eigenvector from the solution of Equation 3.9 and $\lambda^{(i)}$ is the corresponding eigenvalue. $\lambda^{(i)}$ is often considered a measure of the usefulness of the corresponding mode $\vec{\phi}_i(\vec{x})$ for approximating the given dataset of potential solution fields. Therefore, a common procedure (as was done herein) is to only use the m modes ($m < n$) with the highest corresponding eigenvalues, for any subsequent solution approximation, and the remaining modes are discarded (The present work uses the set with corresponding eigenvalues that represent around 99% of the total sum of the n eigenvalues). See [22] and [63] for additional details on POD basis generation.

3.4.2 ROM for Flow Around a Stationary Cylinder

Once the POD modes are obtained, the Navier-Stokes equations can be projected onto these modes using a standard Galerkin approach. Starting with weak form of the BVP:

$$\int_{\Omega} \rho \vec{v}(\vec{x}) \cdot \frac{\partial}{\partial t} \vec{u}(\vec{x}, t) d\vec{x} + \int_{\Omega} \rho \vec{v}(\vec{x}) \vec{u}(\vec{x}, t) \nabla \cdot \vec{u}(\vec{x}, t) d\vec{x} - \int_{\Omega} p \nabla \cdot \vec{v}(\vec{x}) d\vec{x} + \int_{\Omega} \mu \nabla \cdot \vec{v}(\vec{x}) \nabla \cdot \vec{u}(\vec{x}, t) d\vec{x} = 0. \tag{3.12}$$

Note that in the formulation used here, the POD modes are created from an ensemble of fluid velocity fields (sampled at various times and/or with varying input parameters) with the average velocity of the ensemble subtracted from each field as:

$$\{\vec{u}(\vec{x}, \vec{\gamma}_k) - \vec{\bar{u}}(\vec{x})\}_{k=1}^{n},$$

with

$$\vec{\bar{u}}(\vec{x}) = \frac{1}{n} \sum_{j=1}^{n} \vec{u}(\vec{x}, \vec{\gamma}_j),$$

To implement the POD modes derived from this ensemble into the above weak form to create a ROM, all that is then necessary is to apply the m obtained vector modes, $\{\vec{\phi}_j\}_{j=1}^{m}$, as the test and trial functions such that:

$$\vec{v}(\vec{x}) = \vec{\phi}_q(\vec{x}), \quad \text{for} \quad q = 1, 2, ..., m, \tag{3.13}$$

and

$$\vec{u}(\vec{x}, t) = \vec{\bar{u}}(\vec{x}) + \sum_{r=1}^{m} a_r(t)\vec{\phi}_r(\vec{x}), \tag{3.14}$$

where a_r is the modal coefficient corresponding to the r^{th} POD mode (i.e., the coefficients to be solved for in the ROM velocity numerical approximation). Noting that if the modes are generated from an ensemble that assumes incompressibility (as is the case herein), then the modes will be divergence-free. Substituting equation 3.14 into Equation 3.12, and using product rule and divergence theorem results in the following equation:

$$\int_{\Omega} \rho\vec{\phi}_q(\vec{x})(\frac{\partial}{\partial t}\vec{u}(\vec{x}, t)+\vec{u}(\vec{x}, t)\nabla\cdot\vec{u}(\vec{x}, t))+\mu\nabla\cdot\vec{\phi}_q(\vec{x})\nabla\cdot\vec{u}(\vec{x}, t)d\vec{x}-\int_{\Gamma} p(\vec{x}, t)\vec{\phi}_q(\vec{x})\cdot\vec{n}(\vec{x})d\vec{x} = 0, \quad for \quad q = 1, 2, \tag{3.15}$$

where $\vec{n}(\vec{x})$ represents the normal vector to each boundary.

The second integral in Equation 3.15, which is over the boundaries, requires careful consideration since it involves the pressure term. If the POD modes are symmetric, the inlet fluxes and outlet fluxes will be equal and opposite, and the second integral in Equation 3.15 is eliminated. As it will be discussed later, for the present work the POD modes will consistently be symmetric with respect to the horizontal line passing through the center of the cylinder.

Substituting the solution expansion (Equation 3.14) into Equation 3.15, a nonlinear evolution equation for the coefficients can be obtained as:

$$\rho\dot{a}_q + \sum_{s=1}^{m}\sum_{r=1}^{m}(A_{qrs}a_r a_s + B_{qr}a_r) + C_q = 0, \quad \text{for} \quad q = 1, 2, ..., m, \tag{3.16}$$

where

$$A_{qrs} = \int_{\Omega} \vec{\phi}_q(\vec{x}) \cdot (\vec{\phi}_r(\vec{x}) \cdot \nabla)\vec{\phi}_s(\vec{x})d\vec{x}, \tag{3.17}$$

$$B_{qr} = \int_{\Omega} \vec{\phi}_q(\vec{x}) \cdot (\vec{\bar{u}}_m(\vec{x}) \cdot \nabla) \vec{\phi}_r(\vec{x}) d\vec{x} + \vec{\phi}_q(\vec{x}) \cdot (\vec{\phi}_r(\vec{x}) \cdot \nabla) \vec{\bar{u}}_m(\vec{x}) d\vec{x} + \int_{\Omega} \nabla \cdot \vec{\phi}_q(\vec{x}) \nabla \cdot \vec{\phi}_r(\vec{x}) d\vec{x}, \quad (3.18)$$

and

$$C_q = \int_{\Omega} \vec{\phi}_q(\vec{x}) \cdot (\vec{\bar{u}}_m(\vec{x}) \cdot \nabla) \vec{\bar{u}}_m(\vec{x}) d\vec{x} + \int_{\Omega} \nabla \cdot \vec{\phi}_q(\vec{x}) \nabla \cdot \vec{\bar{u}} d\vec{x}. \quad (3.19)$$

The initial condition for Equation 3.16 is defined by inner product of each mode by the FOM solution field at time zero and can be shown as:

$$a_q|_{t=0} = \int_{\Omega} \vec{\phi}_q(\vec{x}) \cdot \vec{u}(\vec{x}, t)|_{t=0} \, d\vec{x}. \quad (3.20)$$

The ordinary differential equation defined by Equation 3.16 can then be solved with any standard nonlinear ordinary differential equation solution method to determine the values of each modal coefficient, $a_q(t)$, over the time domain of the problem considered, and thereby approximate the flow field through a ROM.

3.4.3 ROM for Flow Around a Rotating Cylinder

For the case when the BVP involves a rotating cylinder, the boundary conditions on the cylinder become inhomogeneous and time-dependent. As a consequence, the POD basis functions used in the Galerkin projection are also inhomogeneous on the cylinder boundary, and the second integral in Equation 3.15, which is related to the pressure cannot be eliminated. However, through a manipulation of the ensemble of snapshots (i.e., $\{\vec{u}(\vec{x}, \vec{\gamma}_k)\}_{k=1}^{n}$), a modified set of POD modes (i.e., $\{\vec{\phi}_i(\vec{x})\}_{i=1}^{m}$) that are homogeneous on the cylinder boundary can be obtained.

The first step in creating the modified ensemble of snapshots is to separate the motion of the fluid on the cylinder from the rest of the domain with a new velocity expansion as:

$$\vec{u}(\vec{x}, t) = \vec{u}^c(\vec{x}, t) + \vec{\tilde{u}}(\vec{x}, t), \quad (3.21)$$

where $\vec{u}^c(\vec{x},t)$ is the reference flow field that describes how the control action influences the flow, which is equal to the rotational velocity on the boundary of the cylinder and zero elsewhere as:

$$\vec{u}^c(\vec{x},t) = \begin{cases} \Theta_r(t)\boldsymbol{e_\theta} & \forall x \in \Gamma_c, \\ 0 & \forall x \in \Gamma/\Gamma_c, \end{cases} \tag{3.22}$$

Then, the POD ROM procedure can be applied in a nearly identical fashion as the previous section, but with the ensemble used to generate the POD modes $\{\vec{\phi}_i(\vec{x})\}_{i=1}^m$ defined as:

$$\{\vec{\hat{u}}(\vec{x},t) - \vec{\bar{u}}(\vec{x})\}_{k=1}^m$$

and now with

$$\vec{\bar{u}}(\vec{x}) = \frac{1}{n}\sum_{j=1}^{n} \vec{\hat{u}}(\vec{x},\vec{\gamma_j})$$

To implement the modified POD modes into the weak form the test functions are defined as before (Equation 3.13), but the trial functions are defined such that:

$$\vec{u}(\vec{x},t) = \vec{u}^c(\vec{x},t) + \vec{\bar{u}}(\vec{x}) + \sum_{r=1}^{m} a_r(t)\vec{\phi}_r(\vec{x}). \tag{3.23}$$

By using this modified decomposition the modes are such that the second integral in Equation 3.15, which includes the pressure term, is again zero. As such the ROM for flow past a rotating cylinder can be shown as:

$$\rho\dot{a}_q + A_{qrs}a_r a_s + B_{qr}a_r + C_q + D_q||\dot{u}_c|| + (E_q + F_{qr}a_r)||u_c|| + G_q(||u_c||)^2 = 0, \quad \text{for} \quad q = 1,2,...,m, \tag{3.24}$$

where

$$D_q = \int_\Omega \phi_{qi}u_{ci}d\vec{x}, \tag{3.25}$$

$$E_q = \mu\int_\Omega \phi_{qi}u_{ck}\bar{u}_{i,k}d\vec{x} + \mu\int_\Omega \phi_{qi}\bar{u}_k u_{ci,k}d\vec{x} + \int_\Omega \phi_{qi,k}u_{ci,k}d\vec{x} - \int_\Omega u_{cq,k}\phi_{qi}d\vec{x}, \tag{3.26}$$

$$F_{qr} = \int_\Omega \phi_{qi}\phi_{rk}u_{ci,k}d\vec{x} + \int_\Omega \phi_{qi}u_{ck}\phi_{rk,i}d\vec{x}, \tag{3.27}$$

$$G_q = \int_\Omega \phi_{qi}u_{ci}u_{ci,i}d\vec{x}, \tag{3.28}$$

Note that the coefficients defined in Equations 3.25 - 3.28 are the additional terms due to the rotation of the cylinder, while the remaining terms match those defined in Equations 3.17-3.19. Lastly, the initial condition for Equation 3.24 is as follows:

$$a_q|_{t=0} = \int_\Omega \phi_{qi} \left(u_i|_{t=0} - u_i^c|_{t=0} - \bar{u}_i(\vec{x})\right) \, d\vec{x}, \quad \text{for} \quad q = 1, 2, ..., m. \tag{3.29}$$

3.5 UTILIZATION OF ROM FOR OPTIMAL CONTROL SOLUTION

In order to utilize the ROM for the solution of the optimal control problem, the objective function (Equation 3.8) must first be converted to be in terms of the POD modal coefficients (i.e., a_i) . Note that the velocity field can be obtained from the ROM (Equation 3.24), but the pressure needs to somehow be calculated to account for its effect on the drag coefficient. In many of the recent similar works [14], the effect of pressure on drag is neglected, and instead a drag-related cost functional is minimized that quantifies the reduction of the wake unsteadiness (i.e. the energy contained in the wake). Alternatively in present work, the effect of pressure is taken into account by first calculating the pressure field from the pressure Poisson equation (PPE). The PPE is derived from the momentum equation by taking the divergence of Equation 3.1 and applying the divergence free condition (Equation 3.2) to produce the following:

$$p_{,jj} = \left(u_k u_{i,k}\right)_{,i}. \tag{3.30}$$

The PPE BVP can be solved through any preferred method (finite difference was used in the present study), noting that the boundary conditions are the same as the boundary conditions for the original BVP (Equations 3.1 and 3.2). After calculating the pressure field from the velocity fields provided by the ROM using PPE, the total drag coefficient over the surface of the cylinder can be calculated as follows:

$$C_D(t) = 2 \int_0^{2\pi} p n_1 d\theta - \frac{2}{Re} \int_0^{2\pi} u_{1,i} n_i d\theta. \tag{3.31}$$

Since the pressure field is obtained from the velocity field, both fields depend upon the POD modal coefficients, and therefore the entire drag coefficient can be thought of as a function of modal coefficients. Thus the optimal control problem can be formulated as a ODE-constrained optimization problem using the objective functional defined previously by Equation 3.8 as follows:

$$\begin{aligned} \underset{c}{\text{minimize}} \quad & J(\boldsymbol{a}, \boldsymbol{c}) \\ \text{subject to} \quad & \boldsymbol{N}(\boldsymbol{a}, \boldsymbol{c}) = 0, \end{aligned} \tag{3.32}$$

where $\boldsymbol{a}$ is the vector of m modal coefficients and $\boldsymbol{c}$ is the vector of control parameters ($\boldsymbol{c} = [A, \omega]^T$), and the constraint $\boldsymbol{N}(\boldsymbol{a}, \boldsymbol{c})$ corresponds to the ROM system of m ODEs for the forward problem of flow past a rotating cylinder (Equation 3.24). In the present work this optimization problem was solved using a conjugate gradient optimization method and the adjoint method as described in the following.

3.5.1 Adjoint Method

The optimization problem in Equation 3.32 can be written equivalently as the minimization of the following Lagrangian functional:

$$\boldsymbol{L}(\boldsymbol{a}, \boldsymbol{c}, \boldsymbol{\zeta}) = \frac{1}{T} \int_0^T \left(\hat{J}(\boldsymbol{a}, \boldsymbol{c}) - \sum_{i=1}^{m} \zeta_i N_i(\boldsymbol{a}, \boldsymbol{c}) \right) dt, \tag{3.33}$$

where $\hat{J}(\boldsymbol{a}, \boldsymbol{c})$ is the sum of instantaneous total drag coefficient and the work done by the forcing resource in terms of the modal coefficients and the control parameters, ζ_i is the i^{th} Lagrange multiplier to enforce the ODE constraints. As explained in [45], the optimal solution is the stationary point of the Lagrangian, which can be defined by setting the total variation of the Lagrangian to zero as:

$$\delta \boldsymbol{L} = \sum_{i=1}^{m} \left(\frac{\partial \boldsymbol{L}}{\partial a_i} \delta a_i \right) + \frac{\partial \boldsymbol{L}}{\partial \boldsymbol{c}} \delta \boldsymbol{c} + \sum_{i=1}^{m} \left(\frac{\partial \boldsymbol{L}}{\partial \zeta_i} \delta \zeta_i \right) = 0, \tag{3.34}$$

where $\delta \boldsymbol{a}$, $\delta \boldsymbol{c}$, and $\delta \boldsymbol{\zeta}$ are arbitrary variations of the respective variables. Since each term in the total variation is independent of one another, the three component variations can be considered and set to zero individually. Setting the first variation of $\boldsymbol{L}$ with respect to the

Lagrange multiplier $\boldsymbol{\zeta}$ equal to zero recovers the ROM ODEs (Equation 3.24). Setting the first variation of $\boldsymbol{L}$ with respect to the modal coefficients equal to zero results in the following adjoint equation:

$$\frac{d\zeta_i(t)}{dt} = -a_i(t) - \sum_{j=1}^{m}\left(B_{ij} + \Theta_r(t)F_{ij} + \sum_{k=1}^{m}(A_{ijk} + A_{jki})a_k(t)\right)\zeta_j(t), \quad \text{for } i = 1, 2, ..., m, \tag{3.35}$$

with the final condition (needed for backward time integration):

$$\zeta_i(T) = 0 \quad \text{for } i = 1, 2, ..., m. \tag{3.36}$$

Taking the derivative of the Lagrangian with respect to the control variables, $\boldsymbol{c}$, results in the following equation, which provides the gradient of the cost functional with respect to the control parameters:

$$\nabla_c J = \frac{1}{T}\int_0^T \left(\sum_{i=0}^{m} L_i(t)\right)\nabla_c\Theta_r(t)dt, \tag{3.37}$$

where,

$$L_i(t) = -D_i\frac{d\zeta_i}{dt} + \alpha\Theta_r(t) + (E_i + \sum_{j=1}^{m} F_{ij} + 2G_i\Theta_r)\zeta_i\,, \quad \text{for } i = 1, 2, ..., m. \tag{3.38}$$

Equation 3.24, along with adjoint equation (Equation 3.35) and optimality condition equation (Equation 3.37), lead to a system of equations that need to be solved simultaneously to solve the optimal control problem. The iterative procedure for solving this optimal control problem is to first guess a vector of control parameters, and then solve the state equation (Equation 3.24) to obtain modal coefficients, $\boldsymbol{a}$. Then, using modal coefficients, one can solve Equation 3.35 for the adjoint variable, and the gradient of the functional can be obtained from Equation 3.37. Using the estimate of the gradient, the vector of control parameters can be updated. In the present work, the conjugate gradient method [15] was used to update the control parameters at each iteration as follows:

$$\boldsymbol{c}^{(n+1)} = \boldsymbol{c}^{(n)} + r^{(n)}\boldsymbol{d}^{(n)}, \tag{3.39}$$

where

$$\boldsymbol{d}^{(n)} = -\nabla_c J^n + \theta^{(n)}\boldsymbol{d}^{(n-1)}, \tag{3.40}$$

where θ coefficients are given by the following equation:

$$\theta^{(n)} = \frac{||\nabla_c J^{(n)}||^2}{||\nabla_c J^{(n-1)}||^2} \tag{3.41}$$

The parameter $r^{(n)}$ in Equation 3.39 represents the relaxation factor, which aids in convergence of the optimization process.

3.6 RESULTS AND DISCUSSION

To evaluate the capability of the optimal control strategy with reduced-order modeling, the example case utilized throughout the formulation of drag coefficient reduction for flow past a single cylinder with its rotation controlled was first analyzed. Then, to examine the more general applicability of the control strategy presented to more complex systems, the algorithm was extended to an example case of flow past two cylinders (specifics detailed in Section 3.6.3).

For both example cases the inlet velocity was taken to be $2 \times 10^{-4} m/s$, which yields a Re number of 200. The standard Unsteady Reynolds Averaged Navier Stokes (URANS) CFD approach [35] was used as the full-order model to generate the snapshot ensemble provided to POD for the examples. In addition, the control parameters of A and ω were assumed to be within the range of $[0.1, 5]$ and $[0.01, 1]$, respectively, for the example cases. Note that in practice the range of control parameters depends on the available forcing source, but for the numerical tests herein the aforementioned intervals for these parameters were chosen arbitrarily.

3.6.1 Snapshot Generation and POD Modes for a Single Cylinder

The snapshot sets were generated by sampling the space of the control parameters and then taking 10 velocity fields equally spaced in time over one complete vortex shedding period from the full-order model for each control parameter set. For the single cylinder test case, the snapshot parameters included a stationary cylinder (i.e., $A = \omega = 0$) as well as every

contribution of five values of the forcing amplitude (A) and four values of forcing frequency (ω), with both sampling uniformly spaced within the specified parameter ranges. Therefore the ensemble of snapshots provided for the single cylinder example has 210 elements (200 with a rotating cylinder and 10 with a stationary cylinder).

To first examine the effect of the cylinder rotation on the POD results from the flow fields (i.e., the coherent structures), Figure 3.2 compares the percent cumulative energy of the 10 modes obtained from decomposing only the 10 snapshots for the stationary cylinder along with the modes obtained from decomposing only the 10 snapshots for the cylinder with a rotational velocity of $\Omega(t) = 1.73\sin(0.505t)$. Note that the rotating cylinder results for the chosen forcing parameters were representative of the results for all forcing parameter sets considered. The percent cumulative energy is defined as the ratio of the total energy (i.e., sum of the corresponding eigenvalues) of the set of the highest energy modes up to the given mode number to the total energy of all modes. Of interest is that the percent cumulative energy of the stationary cylinder converges to 100% significantly faster than that for the rotating cylinder. For example, three POD modes would be sufficient to capture 99% of the energy of the stationary cylinder, whereas 7 modes would be necessary to capture 99% of the energy of the rotating cylinder. This behavior illustrates the significant increase in the complexity of the flow fields obtained from the rotating cylinder compared to the stationary cylinder, and the resulting need to include significantly more modes to accurately capture the behavior of the latter case with a ROM.

3.6.2 Optimal Control Results for Flow Past a Sing Cylinder

The specified set of 210 snapshots was decomposed with POD, and the 34 highest-energy modes were used to create a ROM for the optimization procedure of flow past a single cylinder (as detailed in Sections 3.4 and 3.5). Three scenarios for the objective function (Equation 3.8) were considered based on different values of α (i.e., different importance weighting for minimizing the energy used to rotate the cylinder). First, α was set to zero, which completely neglects the required input energy for rotation. Next, α was arbitrarily assigned a value of 0.5, and then 1.0. To be consistent, the optimization process for each case was

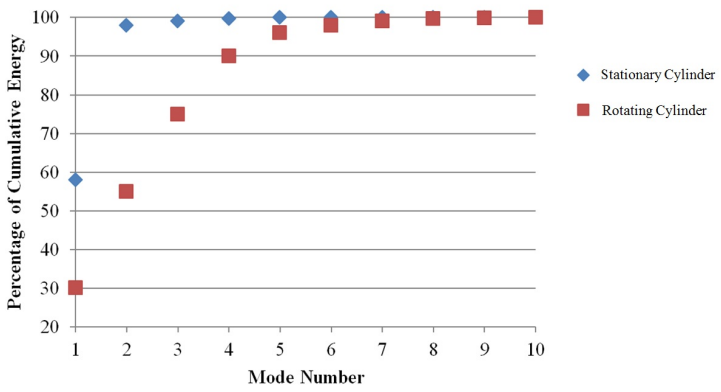

Figure 3.2: The convergence of the cumulative energy of POD modes for the stationary cylinder and one rotating cylinder with rotational velocity of $\Omega(t) = 1.73\sin(0.505t)$.

set to terminate at a fixed number of iterations of 40. Also, the initial guess for the control parameters of each trial was set to $A = 0.1$ and $\omega = 0.01$. An important note is that the entire ROM optimization process (80 ROM analyses) for each trial required approximately one hour of total computing time, while a single full-order model analysis of the flow past a rotating cylinder for one vortex shedding period required more than 24 hours on the same machine. Thus, there was multiple orders of magnitude reduction in the computing cost by using a ROM in place of a full-order model within the optimization process.

Figure 3.3 shows the iterative decrease in the cost functional over the optimization process for the three trials. The cost functional for the trial with $\alpha = 0$ appeared to be converging to a final solution after the 40 iterations. However, although the other two trials that account for the rotation energy show a substantial decrease in the respective cost functionals over the optimization process, neither appears to be at a similar convergence point after 40 iterations. To compare the final solutions of the three trials, Table 3.1 shows the estimate of the optimal control parameters after the 40 iterations, along with the percent reduction in the total cost functional relative to the initial guess (RC), and the percent reduction in the drag coefficient relative to a stationary cylinder (RD) for each trial. All three trials produced similar relatively large reductions in their respective total cost functionals, which

further highlights the success of the optimization procedure. More importantly, Table 3.1 shows the significance of the weight given to the energy cost of rotating the cylinder (α). All three values of the weighting produced significantly different final estimates for the rotation control parameters. Thus, as would be expected, as α increases and more importance is placed on the energy cost of rotating the cylinder, the amount of reduction achieved in the drag coefficient substantially decreases.

3.6.3 Extension to Control of Flow Past Two Cylinders

Figure 3.4 shows a schematic of the test case considered for the control of flow past two cylinders. For simplicity, both cylinders were taken to be the same size and the two cylinders were assumed to be controlled with the same amplitude and frequency, so that the control parameters still consisted of only A and ω and Equation 3.7 was applied to both cylinders. The cost functional can be extended for this two-cylinder example to account for the drag and energy of both cylinders as:

$$J(A,\omega) = \int_0^T (C_{D_1}(t) + C_{D_2}(t))dt + 2\alpha \int_0^T \Omega^* t dt, \tag{3.42}$$

where C_{D_1} and C_{D_2} are drag coefficients corresponding to the cylinder nearest to the inlet and the cylinder nearest to the outlet respectively.

The same procedure described for the single cylinder was applied to create the ROMs and perform the control optimization for this two-cylinder case. However, due to the increase in the complexity of the flow fields for this second example, it was necessary to generate more snapshots than for the previous example to ensure the ROMs maintained sufficient accuracy. 10 velocity fields were again sampled uniformly over a single vortex shedding period for each set of control parameters, and the first set was again the case of both cylinders being stationary. Then, snapshots were generated for every combination of 10 values of the forcing amplitude and eight values of the forcing frequency sampled uniformly within the specified parameter ranges. The total ensemble of snapshots provided for POD of the two-cylinder example had 810 elements. The set of 810 snapshots was decomposed with POD, and the

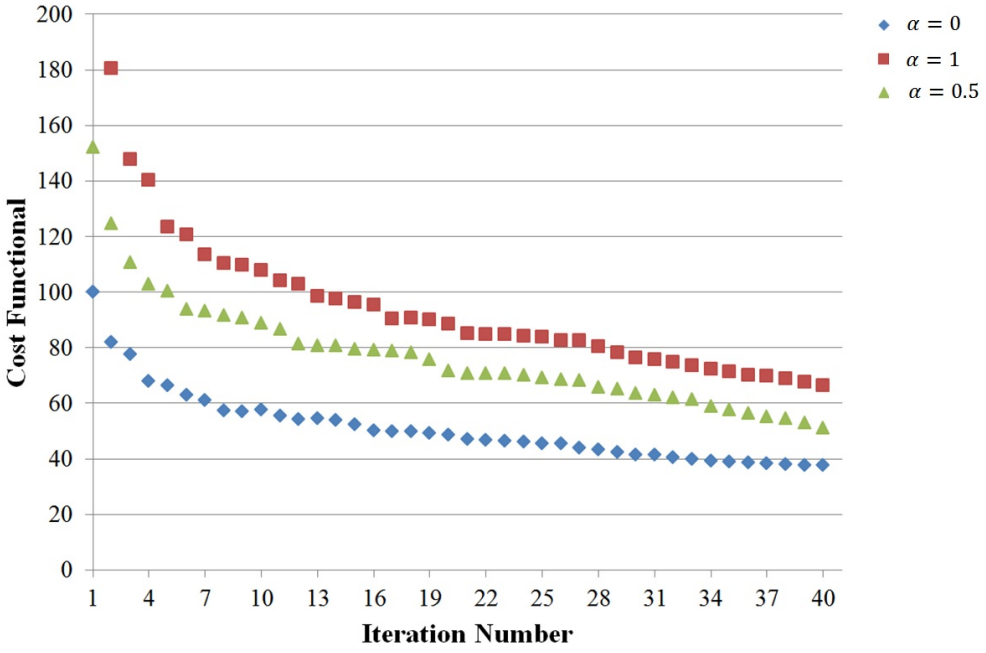

Figure 3.3: Evolution of the cost functional at each iteration of the optimization for three scenarios of the weight parameter α.

Table 3.1: Summary of the control parameters at the end of the optimization process, corresponding relative cost functional reduction (RC), and relative drag reduction (RD) for each scenario of the optimal control of flow past a single cylinder.

Scenario	A	ω	RC (%)	RD (%)
$\alpha = 0$	2.54	0.67	62.35	27.61
$\alpha = 0.5$	1.69	0.55	66.44	17.44
$\alpha = 1$	0.77	0.34	63.95	9.28

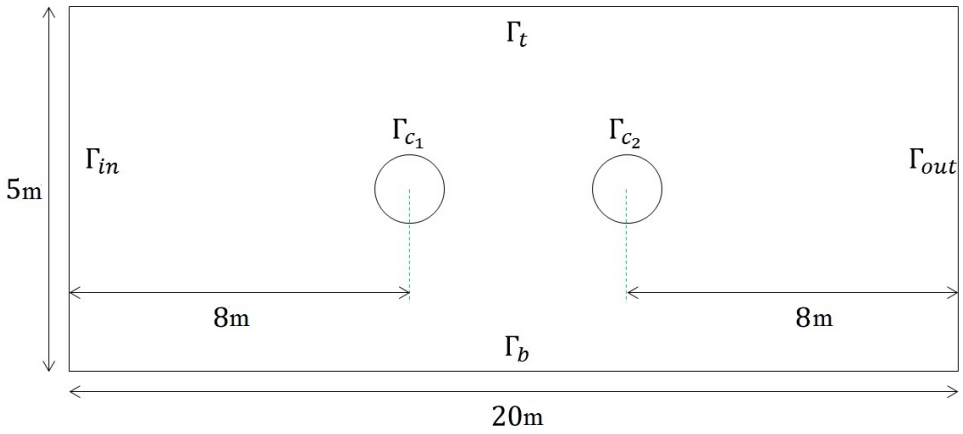

Figure 3.4: Schematic for flow past two cylinders in a channel.

47 highest-energy modes were used to create a ROM for the optimization procedure of flow past two cylinders. For this example, only two scenarios for the objective functional were considered: $\alpha = 0$ (i.e., neglecting energy cost) and $\alpha = 1$. The same initial guess for the control parameters as the previous example was used of $A = 0.1$ and $\omega = 0.01$, and again the optimization was terminated after 40 iterations.

Figure 3.5 shows the iterative decrease in the cost functional over the optimization process for the two trials. Although the change in the cost functional for both trials appeared to be slowing towards the end of the optimization process, neither trial appeared to be converging to a final solution estimate in the same manner as the first trial of the previous example. However, the optimization process was again successful in decreasing the cost functional in both trials, and the rate of this decrease was similar to the previous example. Table 3.2 shows the estimate of the optimal control parameters after the 40 iterations, along with the percent reduction in the total cost functional relative to the initial guess, and the percent reduction in the drag coefficient relative to the two cylinders being stationary for both trials. Again, both trials produced relatively large reductions in their respective total cost functionals, and the change in the weighting parameter significantly affected the optimal control parameter estimates. In contrast, both the drag coefficient reduction when the energy cost was ignored

and the difference between the drag coefficient reduction when the energy was included and when it was ignored increased compared to the previous single cylinder example. The increase in the drag coefficient reduction when ignoring energy cost is reasonable, since with two cylinders a larger portion of the flow field can be affected than with one. To interpret the change in outcome when the energy cost is included, it is important to note that when two cylinders are in line, the drag force on the downstream cylinder is significantly lower than that of the upstream cylinder [62]. Therefore, the effect of the rotation of both cylinders on the flow field is not equal, even though both cylinders were forced to have the same rotational control, resulting in an increase in the energy cost for a disproportionate decrease to the drag coefficient reduction in contrast to the single cylinder example.

Although not considered herein for the sake of brevity, a relatively simple solution to improve the efficiency of the two-cylinder example could be to allow the two cylinders to be controlled independently. In particular, the contribution of the drag coefficient of the downstream cylinder on the total drag coefficient depends on the distance between the cylinders, and it reaches a maximum when $\frac{L}{D} = 3.6$, where L is the distance between the cylinders and D is the diameters of the cylinders [62]. Hence, when $\frac{L}{D}$ is relatively far from 3.6, the two cylinders could be set to be controlled independently, and a new cost functional that accounts for the rotational energy cost independently for each cylinder could be utilized for the optimization.

3.7 CONCLUSIONS

An approach was presented and numerically evaluated to utilize proper orthogonal decomposition-based reduced-order modeling to estimate a solution for optimal control of rotary cylinders for drag reduction in fluid flows. This approach utilized the Galerkin projection ROM method, and the ROM formulation of the control objective included the effect of the pressure field in quantifying the cylinder drag, in addition to the effect of the velocity gradient. Through two test cases, one involving flow past a single cylinder and the other involving flow past two in-line cylinders, the strategy was capable of finding control solutions to significantly

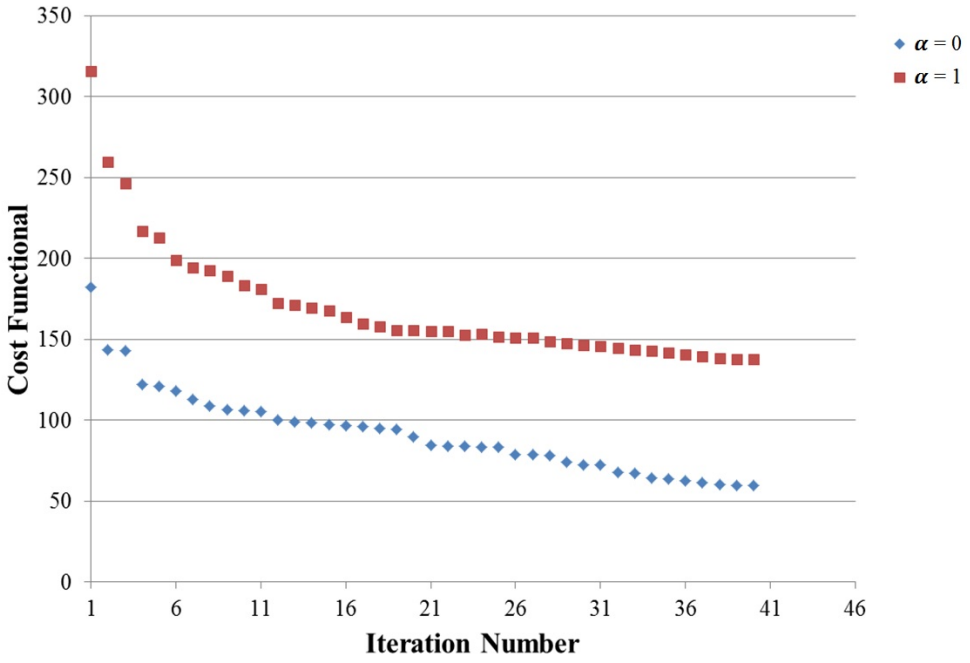

Figure 3.5: Evolution of the cost functional at each iteration of the optimization for two scenarios of the weight parameter α.

Table 3.2: Summary of the control parameters at the end of the optimization process, corresponding relative cost functional reduction (RC), and relative drag reduction (RD) for each scenario of the optimal control of flow past two cylinders.

Scenario	A	ω	RC (%)	RD (%)
$\alpha = 0$	3.87	0.71	67.40	34.44
$\alpha = 1$	0.65	0.32	56.50	7.39

reduce the drag coefficient on the cylinder(s) with substantially less computational cost than if full-order modeling had been used. Furthermore, the tradeoff between the conflicting objectives of reducing the drag while minimizing the energy required for the control process was revealed with the ROM-optimization procedure as well. This tradeoff was particularly evident for the case of flow past two in-line cylinders, where the energy cost of controlling the downstream cylinder was far greater than the relative drag reduction. However, it is expected that significant improvement in the overall optimization of a multiple-cylinder system would be obtained through a slight modification of the formulation to allow for independent control of each cylinder.

4.0 CURRENT CAPABILITIES AND FUTURE DIRECTIONS

Throughout the present work proper orthogonal decomposition-based reduced-order modeling was utilized and evaluated for the solution of computationally expensive problems in computational mechanics. Toward this end, two different types of problems were considered: (1) relatively numerically simple (i.e., inexpensive) problems with high dimensional parameter spaces and (2) numerically more complex problems with low dimensional parameter spaces. For the first type of problems, even though solving the full-order model of the system is not considered to be computationally expensive for a specific set of input parameters, since the space of input parameters is large, several orders of magnitude of full-order model simulations are often required to solve an inverse/optimization problem for such a system which makes the process computationally expensive and reduced-order modeling required. For the second type of problems, the full-order model simulation of the system is itself computationally expensive, and even though a relatively small number of full-order model simulation would be required to solve an inverse/optimization problem, the total computational cost of the process makes the use of full-order modeling prohibitive and some form of model reduction is necessary.

In the context of the first class of problems, a generally applicable algorithm for the iterative generation of data ensembles to efficiently create accurate ROMs for use in computational approaches to approximate inverse problem solutions was developed and numerically evaluated. The algorithm considers characteristics of the problem, rather than *a priori* sampling the parameter space, to generate snapshots. The core hypothesis of the algorithm is that maximizing the diversity, as defined in a measurable sense, of the full-order models used to create the ROM will improve the accuracy of the ROM over a broad range of input system parameters. Based on an initial (small) set of snapshots, the algorithm uses snapshot

correlation to quantify the snapshot diversity with respect to the system input parameters. Then, the algorithm iteratively applies surrogate-model optimization to identify the next set(s) of system input parameters to be evaluated with full-order analyses to create additional "optimal" snapshots. The main advantage of the proposed algorithm is its capability to sample large dimensional parameter spaces. The algorithm automatically determines the regions of the parameter space that need additional sampling to improve approximation capability efficiently. Although the present work examined the capabilities of this algorithm for two numerically simple test cases, the proposed algorithm is potentially capable of creating accurate ROMs for more complex systems to be used in NDT problems, or in general, any type of inverse problem. The proposed algorithm could also have benefit for creating accurate ROMs for numerically complex systems, since the algorithm does not require a large initial ensemble of FOM solution fields (which are computationally expensive to generate). Therefore, the process of creating accurate ROMs for numerically complex systems could be computationally efficient as well.

For the second class of the problems discussed (i.e., numerically complex problems with low dimensional parameter spaces), sampling the parameter space is not as important as it is for the first type of problems, and the focus is on creating accurate ROMs that are valid over a broad range of the system input parameters. To this end, the present work first investigated different approaches of POD-based reduced-order modeling for the numerically complex problem of flow past a single cylinder and flow past a cluster of four cylinders. Two fundamentally different ROM approaches that similarly utilize a POD basis were evaluated and compared: (1) the Galerkin projection approach, in which the Navier-Stokes equations are projected onto the low dimensional POD basis, and (2) a surrogate modeling approach, in which the governing equations of the system are replaced with a surrogate mapping (e.g., radial basis function interpolation/extrapolation) of the modal coefficients of the POD basis. For predicting responses in time with a fixed Re number for a single cylinder, all of the ROMs were relatively accurate, but the surrogate model ROMs were significantly more accurate than the Galerkin projection ROMs, particularly at the lower values of Re number. Alternatively, for predicting the flow response for varying Re number, the surrogate model approach became ineffectual (errors greater than 100%), while the Galerkin projection ap-

proach increased in error by a relatively small amount compared to prediction with fixed Re number. For the example of flow past a cluster of four cylinders, the accuracy of both ROM approaches was commensurate for predicting responses in time with fixed Re number (i.e., the accuracy of the surrogate model approach decreased significantly), and the maximum error of the ROM approaches increased by only a relatively small amount compared to the single cylinder example. As before, the surrogate model approach was unable to accurately predict variations in Re number, while the Galerkin projection approach was approximately as accurate as for the single cylinder example. In other words, while surrogate modeling performs better than the Galerkin-projection approach for problems that do not have complex POD bases and the original set of snapshots are enriched sufficiently, the Galerkin projection approach maintains the same level of accuracy when it comes to complex problems with a relatively small number of snapshots in the original ensemble. The framework developed in the present work can be extended to more complex problems, such as flow past a bundle of cylinders (e.g., turbulent flow in the lower plenum of a VHTR), and as it was discussed above, for complex geometries, the Galerkin projection approach is a more robust method to create accurate ROMs that are valid over a range of parameters. On the other hand, for numerically complex problems with simple geometries, such as boundary layer flows, shear layer flows, or flow past any bluff body, it is expected that a surrogate modeling method is a more computationally efficient approach to create accurate ROMs (compared to the Galerkin projection method).

Lastly, to study the capability of reduced-order modeling in solving optimization problems for complex systems, an approach for utilizing reduced-order modeling within a computational procedure to optimally control rotary cylinders for drag reduction in fluid flows was developed and numerically evaluated. More specifically, the objective of the optimal control problem considered was reduction of the drag coefficient acting on one or more embedded cylinders in a flow field while simultaneously utilizing the least amount of energy through control of the rotational velocity of the cylinder(s). The effect of the pressure field on the drag on the cylinder(s) was included in the objective, in addition to the effect of the fluid velocity gradient, to provide a physically accurate measure of the drag. The optimal control problem was formulated in terms of the POD modal coefficients and gradient-based

optimization with the adjoint method was used to estimate an optimal control solution. Two simulated case studies were used to evaluate the computational procedure: the first involving flow past a single rotary cylinder and the second involving flow past two in-line rotary cylinders. In all test cases the solution procedure was shown to determine a set of control parameters to substantially reduce the drag coefficient of the system with significantly less computational expense than if standard computational fluid dynamics had been used. In addition, a significant tradeoff was shown between the objective of reducing the drag coefficient and the objective of minimizing the energy cost of rotating the cylinder(s), particularly for the two-cylinder case. The computational procedure to solve the optimal control problem can be potentially applicable to more realistic test cases with more complex geometries. To improve the efficiency of the computational procedure, the forcing resource can be distributed for each cylinder based on its contribution in the total drag coefficient of the system. In other words, if the drag coefficient on cylinder A is always less than the drag coefficient on cylinder B, one can make the search space of the control parameters of cylinder A smaller than the search space for control parameters of cylinder B, thereby improve the efficiency of the optimization process as well as the quality of the control solution obtained.

BIBLIOGRAPHY

[1] Swagato Acharjee and Nicholas Zabaras. A proper orthogonal decomposition approach to microstructure model reduction in rodrigues space with applications to optimal control of microstructure-sensitive properties. *Acta Materialia*, 51(18):5627–5646, 2003.

[2] JD Achenbach. Quantitative nondestructive evaluation. *International Journal of Solids and Structures*, 37(1):13–27, 2000.

[3] OM Alifanov and AV Nenarokomov. Boundary inverse heat conduction problem: algorithm and error analysis. *Inverse Problems in Engineering*, 9(6):619–644, 2001.

[4] Marcılio Alves, Jilin Yu, and Norman Jones. On the elastic modulus degradation in continuum damage mechanics. *Computers & Structures*, 76(6):703–712, 2000.

[5] Wilkins Aquino. An object-oriented framework for reduced-order models using proper orthogonal decomposition (pod). *Computer methods in applied mechanics and engineering*, 196(41):4375–4390, 2007.

[6] Wilkins Aquino and John C Brigham. Self-learning finite elements for inverse estimation of thermal constitutive models. *International Journal of Heat and Mass Transfer*, 49(15):2466–2478, 2006.

[7] Farid Asma and Amar Bouazzouni. Finite element model updating using frf measurements. *Shock and Vibration*, 12(5):377–388, 2005.

[8] Jeanne A Atwell and Belinda B King. Proper orthogonal decomposition for reduced basis feedback controllers for parabolic equations. *Mathematical and computer modelling*, 33(1):1–19, 2001.

[9] Ashutosh Bagchi. Updating the mathematical model of a structure using vibration data. *Journal of Vibration and Control*, 11(12):1469–1486, 2005.

[10] Zhaojun Bai. Krylov subspace techniques for reduced-order modeling of large-scale dynamical systems. *Applied Numerical Mathematics*, 43(1):9–44, 2002.

[11] HT Banks, Michele L Joyner, Buzz Wincheski, and William P Winfree. Real time computational algorithms for eddy-current-based damage detection. *Inverse problems*, 18(3):795, 2002.

[12] Ivan Bartoli, Alessandro Marzani, Francesco Lanza di Scalea, and Erasmo Viola. Modeling wave propagation in damped waveguides of arbitrary cross-section. *Journal of Sound and Vibration*, 295(3):685–707, 2006.

[13] L Cordier Bergmann and JP Brancher. Optimal rotary control of the cylinder wake using pod reduced order model. aiaa paper 2004-2323. In *2nd AIAA Flow Control Conference*, 2004.

[14] Michel Bergmann and Laurent Cordier. Optimal control of the cylinder wake in the laminar regime by trust-region methods and pod reduced-order models. *Journal of Computational Physics*, 227(16):7813–7840, 2008.

[15] Thomas R Bewley, Parviz Moin, and Roger Temam. Dns-based predictive control of turbulence: an optimal benchmark for feedback algorithms. *Journal of Fluid Mechanics*, 447:179–225, 2001.

[16] Jeff Borggaard and Traian Iliescu. Reduced-order modeling for optimization and control of complex flows. Technical report, DTIC Document, 2010.

[17] JC Brigham, W Aquino, FG Mitri, JF Greenleaf, and M Fatemi. Inverse estimation of viscoelastic material properties for solids immersed in fluids using vibroacoustic techniques. *Journal of Applied Physics*, 101(2):023509, 2007.

[18] John C Brigham and Wilkins Aquino. Inverse viscoelastic material characterization using pod reduced-order modeling in acoustic–structure interaction. *Computer Methods in Applied Mechanics and Engineering*, 198(9):893–903, 2009.

[19] John Burkardt, Max Gunzburger, and Hyung-Chun Lee. Centroidal voronoi tessellation-based reduced-order modeling of complex systems. *SIAM Journal on Scientific Computing*, 28(2):459–484, 2006.

[20] Edgar Caraballo, X Yuan, Jesse Little, Marco Debiasi, P Yan, Andrea Serrani, James Myatt, and Mo Samimy. Feedback control of cavity flow using experimental based reduced order model. *AIAA paper*, 5269:2005, 2005.

[21] FN Catbas, T Kijewski-Correa, and AE Aktan. Structural identification (st-id) of constructed facilities–approaches, methods and technologies for effective practice of st-id. In *Am Soc Civ Eng*, 2011.

[22] Anindya Chatterjee. An introduction to the proper orthogonal decomposition. *Current science*, 78(7):808–817, 2000.

[23] F Chinesta, A Ammar, F Lemarchand, P Beauchene, and F Boust. Alleviating mesh constraints: model reduction, parallel time integration and high resolution homogenization. *Computer methods in applied mechanics and engineering*, 197(5):400–413, 2008.

[24] Francisco Chinesta, Pierre Ladeveze, and Elías Cueto. A short review on model order reduction based on proper generalized decomposition. *Archives of Computational Methods in Engineering*, 18(4):395–404, 2011.

[25] CL Chow and June Wang. An anisotropic theory of continuum damage mechanics for ductile fracture. *Engineering Fracture Mechanics*, 27(5):547–558, 1987.

[26] Saptarshi Das, Shantanu Das, and Amitava Gupta. Fractional order modeling of a phwr under step-back condition and control of its global power with a robust controller. *Nuclear Science, IEEE Transactions on*, 58(5):2431–2441, 2011.

[27] AE Deane, IG Kevrekidis, G Em Karniadakis, and SA Orszag. Low-dimensional models for complex geometry flows: Application to grooved channels and circular cylinders. *Physics of Fluids A: Fluid Dynamics (1989-1993)*, 3(10):2337–2354, 1991.

[28] Joris Degroote, Jan Vierendeels, and Karen Willcox. Interpolation among reduced-order matrices to obtain parameterized models for design, optimization and probabilistic analysis. *International Journal for Numerical Methods in Fluids*, 63(2):207–230, 2010.

[29] Scott W Doebling, Charles R Farrar, Michael B Prime, et al. A summary review of vibration-based damage identification methods. *Shock and vibration digest*, 30(2):91–105, 1998.

[30] Sergio L dos Santos e Lucato, Ju Wang, P Maxwell, RM McMeeking, and AG Evans. Design and demonstration of a high authority shape morphing structure. *International journal of solids and structures*, 41(13):3521–3543, 2004.

[31] Qiang Du, Vance Faber, and Max Gunzburger. Centroidal voronoi tessellations: applications and algorithms. *SIAM review*, 41(4):637–676, 1999.

[32] Georges Dumont and Christofer Kühl. Finite element simulation for design optimisation of shape memory alloy spring actuators. *Engineering computations*, 22(7):835–848, 2005.

[33] Marco Fahl. *Trust-region methods for flow control based on Reduced Order Modeling*. PhD thesis, Ph. D. thesis, Trier university, 2000.

[34] Li-Hao Feng, Jin-Jun Wang, and Chong Pan. Proper orthogonal decomposition analysis of vortex dynamics of a circular cylinder under synthetic jet control. *Physics of Fluids (1994-present)*, 23(1):014106, 2011.

[35] INC Fluent. Fluent 6.3 users guide. *Fluent documentation*, 2006.

[36] M Gad-el Hak. Flow control: Passive, active and reactive flow management, 2000.

[37] B Galletti, CH Bruneau, Luca Zannetti, and Angelo Iollo. Low-order modelling of laminar flow regimes past a confined square cylinder. *Journal of Fluid Mechanics*, 503:161–170, 2004.

[38] EA Gillies. Low-dimensional control of the circular cylinder wake. *Journal of Fluid Mechanics*, 371(1):157–178, 1998.

[39] David Edward Goldberg et al. *Genetic algorithms in search, optimization, and machine learning*, volume 412. Addison-wesley Reading Menlo Park, 1989.

[40] David González, F Masson, F Poulhaon, A Leygue, Elías Cueto, and Francisco Chinesta. Proper generalized decomposition based dynamic data driven inverse identification. *Mathematics and Computers in Simulation*, 82(9):1677–1695, 2012.

[41] James K Guest and Jean H Prévost. Optimizing multifunctional materials: design of microstructures for maximized stiffness and fluid permeability. *International Journal of Solids and Structures*, 43(22):7028–7047, 2006.

[42] Serkan Gugercin and Athanasios C Antoulas. A survey of model reduction by balanced truncation and some new results. *International Journal of Control*, 77(8):748–766, 2004.

[43] Hasan Gunes, Sirod Sirisup, and George Em Karniadakis. Gappy data: To krig or not to krig? *Journal of Computational Physics*, 212(1):358–382, 2006.

[44] Steve R Gunn. Support vector machines for classification and regression. *ISIS technical report*, 14, 1998.

[45] MD Gunzburger. Inverse design and optimization methods. *Von Karman Institute for Fluid Dynamics Lecture Series*, 5, 1997.

[46] Sangbo Han and Brian Feeny. Application of proper orthogonal decomposition to structural vibration analysis. *Mechanical Systems and Signal Processing*, 17(5):989–1001, 2003.

[47] Francois M Hemez and Charbel Farhat. Locating and identifying structural damage using a sensitivity-based model updating methodology. In *AIAA/ASME/ASCE/AHS/ASC 34th Structures, Structural Dynamics, and Materials Conference*, volume 1, pages 2641–2653, 1993.

[48] Philip Holmes, John L Lumley, and Gal Berkooz. *Turbulence, coherent structures, dynamical systems and symmetry*. Cambridge university press, 1998.

[49] Kazufumi Ito and SS Ravindran. A reduced-order method for simulation and control of fluid flows. *Journal of computational physics*, 143(2):403–425, 1998.

[50] Ruichen Jin, Wei Chen, and Timothy W Simpson. Comparative studies of metamodelling techniques under multiple modelling criteria. *Structural and Multidisciplinary Optimization*, 23(1):1–13, 2001.

[51] Michele L Joyner. A numerical study of the pod method in nde. *Applied mathematics and computation*, 174(1):732–754, 2006.

[52] John Kim and Thomas R Bewley. A linear systems approach to flow control. *Annu. Rev. Fluid Mech.*, 39:383–417, 2007.

[53] GA Kopp, JA Ferre, and Francesc Giralt. The use of pattern recognition and proper orthogonal decomposition in identifying the structure of fully-developed free turbulence. *Journal of fluids engineering*, 119(2):289–296, 1997.

[54] K Kunisch and Stefan Volkwein. Galerkin proper orthogonal decomposition methods for a general equation in fluid dynamics. *SIAM Journal on Numerical analysis*, 40(2):492–515, 2002.

[55] Karl Kunisch and Stefan Volkwein. Control of the burgers equation by a reduced-order approach using proper orthogonal decomposition. *Journal of Optimization Theory and Applications*, 102(2):345–371, 1999.

[56] Matthijs Langelaar and Fred van Keulen. Sensitivity analysis of shape memory alloy shells. *Computers & Structures*, 86(9):964–976, 2008.

[57] R Scott Larson and Matthew R Jones. Reduced-order modeling of time-dependent reflectance profiles from purely scattering media. *Journal of Quantitative Spectroscopy and Radiative Transfer*, 109(2):201–209, 2008.

[58] Changhoon Lee, John Kim, David Babcock, and Rodney Goodman. Application of neural networks to turbulence control for drag reduction. *Physics of Fluids (1994-present)*, 9(6):1740–1747, 1997.

[59] F Leibfritz and S Volkwein. Reduced order output feedback control design for pde systems using proper orthogonal decomposition and nonlinear semidefinite programming. *Linear algebra and its applications*, 415(2):542–575, 2006.

[60] Jean Lemaitre and Horst Lippmann. *A course on damage mechanics*, volume 2. Springer Berlin, 1996.

[61] GC Lewin and H Haj-Hariri. Reduced-order modeling of a heaving airfoil. *AIAA journal*, 43(2):270–283, 2005.

[62] Chunlei Liang, George Papadakis, and Xiaoyu Luo. Effect of tube spacing on the vortex shedding characteristics of laminar flow past an inline tube array: a numerical study. *Computers & Fluids*, 38(4):950–964, 2009.

[63] YC Liang, HP Lee, SP Lim, WZ Lin, KH Lee, and CG Wu. Proper orthogonal decomposition and its applicationspart i: Theory. *Journal of Sound and vibration*, 252(3):527–544, 2002.

[64] Erwan Liberge and Aziz Hamdouni. Reduced order modelling method via proper orthogonal decomposition (pod) for flow around an oscillating cylinder. *Journal of Fluids and Structures*, 26(2):292–311, 2010.

[65] T Lieu, C Farhat, and M Lesoinne. Reduced-order fluid/structure modeling of a complete aircraft configuration. *Computer methods in applied mechanics and engineering*, 195(41):5730–5742, 2006.

[66] Thuan Lieu and Charbel Farhat. Adaptation of pod-based aeroelastic roms for varying mach number and angle of attack: Application to a complete f-16 configuration. *AIAA paper*, 7666:2005, 2005.

[67] Thuan Lieu and Charbel Farhat. Adaptation of aeroelastic reduced-order models and application to an f-16 configuration. *AIAA journal*, 45(6):1244–1257, 2007.

[68] Thuan Lieu and Michel Lesoinne. Parameter adaptation of reduced order models for three-dimensional flutter analysis. *AIAA Paper*, 888:2004, 2004.

[69] GR Liu, X Han, and KY Lam. A combined genetic algorithm and nonlinear least squares method for material characterization using elastic waves. *Computer methods in applied mechanics and Engineering*, 191(17):1909–1921, 2002.

[70] GR Liu, WB Ma, and X Han. An inverse procedure for determination of material constants of composite laminates using elastic waves. *Computer Methods in Applied Mechanics and Engineering*, 191(33):3543–3554, 2002.

[71] Søren Nymand Lophaven, Hans Bruun Nielsen, and Jacob Søndergaard. Dace-a matlab kriging toolbox, version 2.0. Technical report, 2002.

[72] Michael JS Lowe. Matrix techniques for modeling ultrasonic waves in multilayered media. *Ultrasonics, Ferroelectrics and Frequency Control, IEEE Transactions on*, 42(4):525–542, 1995.

[73] David J Lucia, Philip S Beran, and Walter A Silva. Reduced-order modeling: new approaches for computational physics. *Progress in Aerospace Sciences*, 40(1):51–117, 2004.

[74] John L Lumley. *Stochastic tools in turbulence*. Courier Corporation, 2007.

[75] John Leask Lumley. The structure of inhomogeneous turbulent flows. *Atmospheric turbulence and radio wave propagation*, pages 166–178, 1967.

[76] Hung V Ly and Hien T Tran. Modeling and control of physical processes using proper orthogonal decomposition. *Mathematical and computer modelling*, 33(1):223–236, 2001.

[77] Glenn E McCreery and Keith G Condie. Experimental modeling of vhtr plenum flows during normal operation and pressurized conduction cooldown. *Idaho National Laboratory, Idaho Falls, Idaho*, 2006.

[78] MD McKay, RJ Beckman, and WJ Conover. A comparison of three methods for selecting values of input variables in the analysis of output from a computer code. *Technometrics*, 42(1):55–61, 2000.

[79] Bijan Mohammadi, Olivier Pironneau, B Mohammadi, and Oliver Pironneau. *Applied shape optimization for fluids*, volume 28. Oxford University Press Oxford, 2001.

[80] Paritosh Mokhasi, Dietmar Rempfer, and Sriharsha Kandala. Predictive flow-field estimation. *Physica D: Nonlinear Phenomena*, 238(3):290–308, 2009.

[81] Bernd R Noack, Konstantin Afanasiev, Marek Morzynski, Gilead Tadmor, and Frank Thiele. A hierarchy of low-dimensional models for the transient and post-transient cylinder wake. *Journal of Fluid Mechanics*, 497:335–363, 2003.

[82] Bernd R Noack, Paul Papas, and Peter A Monkewitz. The need for a pressure-term representation in empirical galerkin models of incompressible shear flows. *Journal of Fluid Mechanics*, 523:339–365, 2005.

[83] Bahram Notghi and John C Brigham. Optimal nondestructive test design for maximum sensitivity and minimal redundancy for applications in material characterization. *Smart Materials and Structures*, 22(12):125036, 2013.

[84] Ziemowit Ostrowski, Ryszard A Białecki, and Alain J Kassab. Estimation of constant thermal conductivity by use of proper orthogonal decomposition. *Computational Mechanics*, 37(1):52–59, 2005.

[85] TA Porsching. Estimation of the error in the reduced basis method solution of nonlinear equations. *Mathematics of Computation*, 45(172):487–496, 1985.

[86] Christophe Prudhomme, Y Maday, AT Patera, G Turinici, DV Rovas, K Veroy, and L Machiels. Reliable real-time solution of parametrized partial differential equations: Reduced-basis output bound methods. *Journal of Fluids Engineering*, 124(1):70–80, 2002.

[87] Mojtaba Rajaee, Sture KF Karlsson, and Lawrence Sirovich. Low-dimensional description of free-shear-flow coherent structures and their dynamical behaviour. *Journal of Fluid Mechanics*, 258:1–29, 1994.

[88] SS Ravindran. A reduced-order approach for optimal control of fluids using proper orthogonal decomposition. *International journal for numerical methods in fluids*, 34(5):425–448, 2000.

[89] SS Ravindran. Control of flow separation over a forward-facing step by model reduction. *Computer methods in applied mechanics and engineering*, 191(41):4599–4617, 2002.

[90] Junuthula Narasimha Reddy. *An introduction to the finite element method*, volume 2. McGraw-Hill New York, 1993.

[91] Vicente J Romero, John V Burkardt, Max D Gunzburger, and Janet S Peterson. Comparison of pure and latinized centroidal voronoi tessellation against various other statistical sampling methods. *Reliability Engineering & System Safety*, 91(10):1266–1280, 2006.

[92] Daniel E Rosario, John C Brigham, and Wilkins Aquino. Identification of material properties of orthotropic elastic cylinders immersed in fluid using vibroacoustic techniques. *Ultrasonics*, 48(6):547–552, 2008.

[93] Clarence W Rowley, Tim Colonius, and Richard M Murray. Model reduction for compressible flows using pod and galerkin projection. *Physica D: Nonlinear Phenomena*, 189(1):115–129, 2004.

[94] CW Rowley. Model reduction for fluids, using balanced proper orthogonal decomposition. *International Journal of Bifurcation and Chaos*, 15(03):997–1013, 2005.

[95] Gianluigi Rozza. Shape design by optimal flow control and reduced basis techniques. 2005.

[96] Gianluigi Rozza, DBP Huynh, and Anthony T Patera. Reduced basis approximation and a posteriori error estimation for affinely parametrized elliptic coercive partial differential equations. *Archives of Computational Methods in Engineering*, 15(3):229–275, 2008.

[97] D Ryckelynck. A priori hyperreduction method: an adaptive approach. *Journal of Computational Physics*, 202(1):346–366, 2005.

[98] AF Saleeb, TE Wilt, NR Al-Zoubi, and AS Gendy. An anisotropic viscoelastoplastic model for compositessensitivity analysis and parameter estimation. *Composites Part B: Engineering*, 34(1):21–39, 2003.

[99] Wilhelmus HA Schilders, Henk A Van der Vorst, and Joost Rommes. *Model order reduction: theory, research aspects and applications*, volume 13. Springer, 2008.

[100] Ryan Schmit and Mark Glauser. Improvements in low dimensional tools for flow-structure interaction problems: using global pod. In *APS Division of Fluid Dynamics Meeting Abstracts*, volume 1, 2003.

[101] GJ Sheu, SM Yang, and WL Huang. Simulating displacement and velocity signals by piezoelectric sensor in vibration control applications. *Smart Materials Research*, 2012, 2012.

[102] Stefan G Siegel, Juergen Seidel, Casey Fagley, DM Luchtenburg, Kelly Cohen, and Thomas McLaughlin. Low-dimensional modelling of a transient cylinder wake using double proper orthogonal decomposition. *Journal of Fluid Mechanics*, 610:1–42, 2008.

[103] Troy R Smith, Jeff Moehlis, and Philip Holmes. Low-dimensional modelling of turbulence using the proper orthogonal decomposition: a tutorial. *Nonlinear Dynamics*, 41(1-3):275–307, 2005.

[104] Alex J Smola and Bernhard Schölkopf. A tutorial on support vector regression. *Statistics and computing*, 14(3):199–222, 2004.

[105] Cyrille Stephan. Sensor placement for modal identification. *Mechanical Systems and Signal Processing*, 27:461–470, 2012.

[106] JA Taylor and MN Glauser. Towards practical flow sensing and control via pod and lse based low-dimensional tools. *Journal of fluids engineering*, 126(3):337–345, 2004.

[107] Jörg F Unger, Anne Teughels, and Guido De Roeck. Damage detection of a prestressed concrete beam using modal strains. *Journal of Structural Engineering*, 131(9):1456–1463, 2005.

[108] Armando Vavalle and Ning Qin. Iterative response surface based optimization scheme for transonic airfoil design. *Journal of aircraft*, 44(2):365–376, 2007.

[109] Mengyu Wang and John C Brigham. Assessment of multi-objective optimization for nondestructive evaluation of damage in structural components. *Journal of Intelligent Material Systems and Structures*, page 1045389X13494933, 2013.

[110] Shuang Wang and John C Brigham. A computational framework for the optimal design of morphing processes in locally activated smart material structures. *Smart Materials and Structures*, 21(10):105016, 2012.

[111] Karen Elizabeth Willcox. *Reduced-order aerodynamic models for aeroelastic control of turbomachines*. PhD thesis, Citeseer, 1999.

[112] Charles HK Williamson. Vortex dynamics in the cylinder wake. *Annual review of fluid mechanics*, 28(1):477–539, 1996.

[113] TI Zohdi. Constrained inverse formulations in random material design. *Computer Methods in Applied Mechanics and Engineering*, 192(28):3179–3194, 2003.